CHAPTER 3

CONCEPT,

PROTOTYPE FABRICATION

AND

METHODOLOGY

3.1 Concept for noninvasive blood glucose measurement:

A truly new technique for non-invasive glucose measurement is the need of hour. Further, none of the existing principles offers enough accuracy to replace finger prick technology [So *et al.* (2014)].

In perspective of addressing this essential requirement, we have introduced a new concept for noninvasive blood glucose measurement in human subjects. Our concept utilizes modulated ultrasound and infrared light based technique for noninvasive measurement of blood glucose levels in the human subjects. The amplitude modulated ultrasonic waves (40 kHz central frequency) utilized here, initiates the process of molecular vibration in the blood tissue medium present inside the fingertip region. Consequently, the molecules will vibrate depending upon their respective physical characteristics like shape, size, molecular weight, and medium in which they are present [Radel *et al.* (2010)]. At the same time, glucose molecule sensitive and specific infrared light of 940 nm passes through that focused ultrasonic vibrational zone for obtaining blood glucose molecule specific vibrational signature patterns. This modulated light response signal is collected by the photo-sensor, further suitably processed using signal processing algorithm to extract the information of blood glucose level.

When the amplitude modulating ultrasonic waves enters inside the measurement site (human finger) the blood constituent molecules under goes vibration phenomenon due to the influence of the amplitude modulated ultrasonic waves. The pressure of the ultrasound waves generates those changes. The intrinsic properties of these molecules present in the blood medium influences the compressibility factor. The shape and size of the molecules present in the blood medium (segment) plays an important role. The magnitude of influence over larger molecules is more as compared to the smaller ones. **Hence, the vibration produced in the blood medium (segment) is based on (i) its spatial arrangement (ii) intrinsic property of the molecules and medium (iii) strength and frequency of the amplitude modulated ultrasonic waves respectively [Radel *et al.* (2010); Coakley (1997)].**

The pressure amplitude of the ultrasonic standing wave has maximum and minimum values twofold above the distance of a unit wavelength [Radel *et al.* (2010); Coakley (1997)]. Within the propagating blood-tissue medium (segment), discontinuities

such as blood molecules (like glucose); cells achieve location specific ultrasonic potential energy due to their presence in the respective ultrasonic zone. The suspended blood molecules (like glucose) start to move and accumulate near to the zone of least ultrasonic potential energy. **For blood molecules (like glucose), these concentrated zones are commonly near to the pressure nodes, distanced from each other by half a wavelength space [Radel *et al.* (2010); Coakley (1997)].**

Now, when the molecular diameter is smaller than the wavelength of propagating ultrasound inside the measurement site, the main force of radiation (F_r) acting on the molecular volume (V_c), positioned by path of distance (z) from the pressure node is obtained from the gradient of the molecular ultrasonic potential energy [Radel *et al.* (2010); Coakley (1997)], and mathematically expressed as:

$$F_r = -\left[\frac{\pi p_o^2 V_c \beta_w}{(2\lambda)}\right] . \phi(\beta, \rho) . \sin(4\pi z/\lambda) \qquad \text{Equation (1)}$$

In this present work, (P_o) stands for peak amplitude of the ultrasonic pressure. (λ) denotes ultrasound wavelength in the suspending segment. (β_w) signify compressibility of the suspending segment and then the $\phi(\beta, \rho)$ function mathematically expressed as [Radel *et al.* (2010); Coakley (1997)]:

$$\phi(\beta, \rho) = \left[\frac{5\rho_c - 2\rho_w}{2\rho_c + \rho_w} - \left(\frac{\beta_c}{\beta_w}\right)\right] \qquad \text{Equation (2)}$$

Where, (β_c) stands for compressibility of the molecules. Notations (ρ_c) and (ρ_w) represent the respective densities of the molecules and the suspending segments respectively [Radel *et al.* (2010); Coakley (1997)].

3.1.1 Absorption spectral analysis:

The well-known Lambert-Beer law applied here to measure the specific absorption (A) property of the glucose molecule at a definite light wave number (v) and mathematically expressed as:

$$A(v) = -\log I(v)/I_0(v) \qquad \text{Equation (3)}$$

In this present work, the (I_o) denotes the background intensity and (I) represents the specific light intensity at the particular wave number (v) of actual measurements [Radel *et al.* (2010)].

When infrared light beam propagates through this ultrasound (amplitude modulated ultrasonic waves) excited (blood tissue complex) optical medium, the IR light sensitive detector captures the glucose molecule based specific vibration signatures. This light interaction phenomenon have been represented by the Beer-Lambert Law in this present work. Hence, as per Urban *et al.* (2010), we achieve the benefit of beam forming at ultrasonic frequency for localizing the radiating force energy towards the particular measurement site (human finger). It initiates the vibration phenomenon at lower frequency such that the displacements are large enough for quantification with the Infrared technique respectively.

In this present work, the signal processing toolbox of MATLAB performs observed signal analysis in FFT (Fast Fourier Transform) domain to extract blood glucose level related embedded information. The peak amplitude variations in FFT domain serves as the functional indicator for measuring actual blood glucose level in study subjects. Hence, this principle aspect forms the basis of our noninvasive blood glucose measurement.

3.2 Prototype fabrication:

Initially, it includes the description regarding ultrasound transducer and light wavelength selection criterions. Afterwards, this portion presents the detailed description of the fabricated prototype (MUS-IR) functional units, in-vitro and in-vivo analysis, test methodologies, Clarke Error Grid and statistical analysis applied in this present work.

3.2.1 Ultrasound frequency selection:

Ultrasonic transducers have found numerous applications in household appliances, medical fields, industries, and oceanography [Se-yuen (2003); Greenslade (1994)].

In the biomedical field, the 40 kHz piezoelectric based ultrasonic transducers aids in enhancing (i) fibrinolysis [Suchkova *et al.* (1998)], (ii) tissue penetration [Suchkova *et al.* (1998), Birnbaum *et al.* (1998)], (iii) clot dissolution [Birnbaum *et al.* (1998); Suchkova *et al.* (2000)], (iv) thrombolysis [Siegel *et al.* (2001)], and (v) wound healing therapy [Voigt *et al.* (2012)].

In this present work, we have selected 40 kHz central frequency based ultrasonic transmitters for providing modulated ultrasonic waves to the

measurement site (fingertip). Further, (i) easy availability, (ii) medically safe and tolerable [Se-yuen (2003); Greenslade (1994)] (iii) less tissue heating [Birnbaum *et al.* (1998); Suchkova *et al.* (2000)], (iv) high skin tissue penetration [Se-yuen (2003); Greenslade (1994)], and (v) low costs of 40 kHz ultrasonic transducers have boosted our motivation for its selection.

Further, Lee *et al.* (2005) applied low frequency ultrasound (20 to 40 kHz) which penetrates rat skin for glucose level monitoring purposes. While this technique have potential but no other similar works seems to be available in literature after that preliminary rat skin based lab experiment.

Radel *et al.* (2010) utilized ultrasonic manipulation techniques to improve sensitivity of infrared spectroscopy for chemical analysis purposes. The amalgamations of both these approaches have generated the new concept for utilization in suspension's chemical analysis. Localized aggregation of particles by application of ultrasound assists in determination of molecule specific infrared signatures of the suspending molecules and medium respectively. Varying the frequency of ultrasonic standing waves controls the location of the particles in the optically sensitive zone in the infrared spectroscopy. They have utilized this approach to quantify polystyrene particle concentrations in methanol suspension and reported promising results.

Encouraged by this above-mentioned approach, in our specific noninvasive glucose measurement application, we have utilized amplitude modulation with central ultrasonic frequency of 40 kHz to initiate required excitation in the particular measurement site (human fingertip) and Infrared light utilized to detect such glucose specific vibrations.

3.2.2 Light wavelength selection:

The composition of human blood is complex and constitutes numerous components in it. Further, glucose molecules exhibit very weak signals [So *et al.* (2012)].

The wavelength selection needs careful and well-judged approaches to overcome this particular phenomenon. The figure 3.1 depicts the absorption spectra of major intracellular absorbers. It represents the molecular extinction coefficients **(ε)** of oxygenated hemoglobin, melanin and the absorption coefficient **(α)** of water respectively. The scarcity of the efficient one-photon absorbers causes the biological cells and tissues

to be optically transparent in the wavelength **(λ)** spectral domain from 700 nm to 1100 nm respectively. Further, the figure 3.2 represents that oxyhemoglobin (HbO_2) and reduced hemoglobin absorption characteristics are comparatively less in Red and NIR spectral bands respectively. Henceforth, the region extending from 700 nm to 1100 nm often termed as "Optical Window" of the living biological tissues [Kulkarni *et al.* (2010); Bashkatov *et al.* (2005); Kong (2000)].

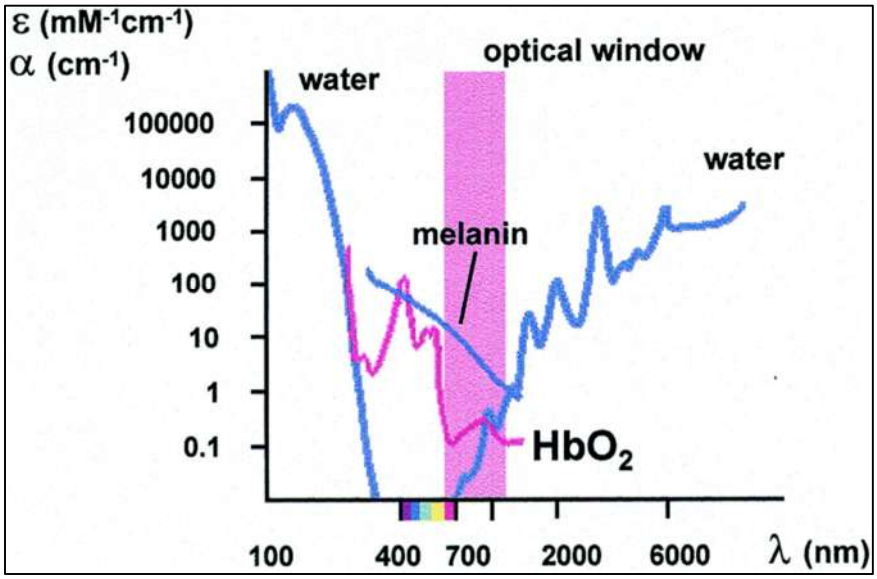

Figure 3.1: Absorption spectra of major intracellular absorbers [Kong (2000)].

Table 3.1: Absorption characteristics corresponding to the stretch and vibration patterns of the bonds present in the glucose molecule [Khalil (1999)].

Wavelength (nm)	Possible Stretch and Vibration	Explanation
939	3*v*OH	Second OH overtone band
1126	3*v*CH	Second harmonic CH overtone band
1408	2*v*OH	First OH overtone band
1536	*v*OH + *v*CH	OH and CH combination band
1688	2*v*CH	CH overtone band
2261	*v*CH + *v*CCH, OCH	Combination of a CH stretch and a CCH,OCH deformation
2326	vCH + vCCH, OCH	

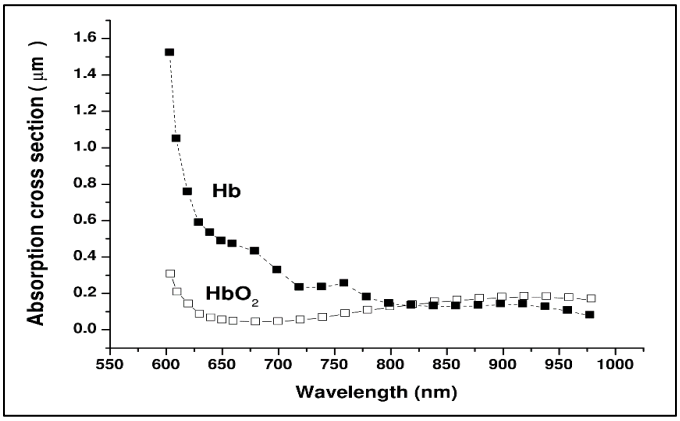

Figure 3.2: Absorption cross-section of oxyhemoglobin and reduced hemoglobin at Red-NIR region [Tuchin (2009); Mendelson (1992); Assendelft (1970)].

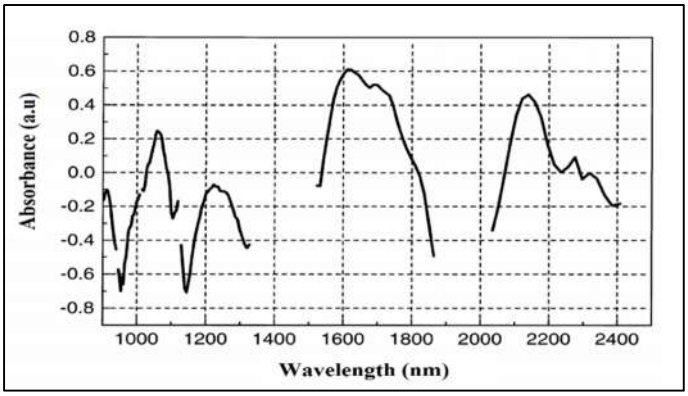

Figure 3.3: Absorption spectrum of glucose dissolved in water within the spectral range extending from 900 nm to 2400 nm [Tenhunen *et al.* (1998)].

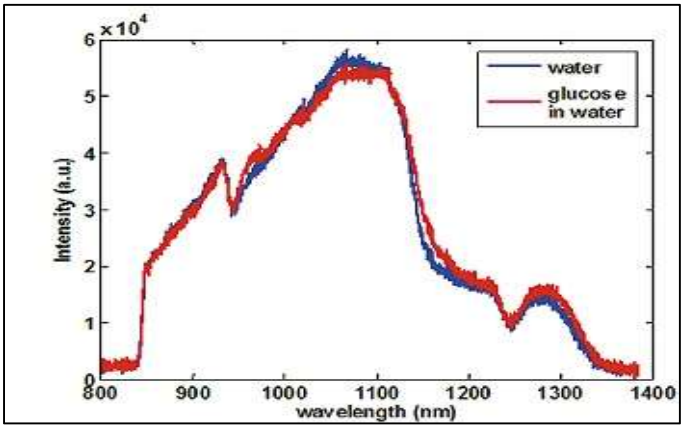

Figure 3.4: Absorption spectrum of water and glucose in water from 800 nm to 1400 nm [Beckers (2013)].

Blood-oxygenations vary blood optical absorption properties [Tuchin (2009); Kulkarni *et al.* (2010)]. The figure 3.2 depicts that the absorption spectrum of oxyhemoglobin and reduced hemoglobin is comparatively low within the spectral wavelength band from 900 nm to 1000 nm respectively [Tuchin (2009); Mendelson (1992)].Hence, blood glucose measurement in this range will have minimal interferences.

The glucose molecules exhibits absorption peaks in the NIR to IR wavelength ranges at 939 nm (very close to 940 nm), 1126 nm, 1408 nm, 1536 nm, 1688 nm, 2261 nm, and 2326 nm band respectively as depicted from figure 3.3 and Table 3.1 respectively [Tenhunen *et al.* (1998); Khalil (1999)]. Similarly, the figure 3.4 depicts that glucose molecules exhibits absorption peaks near to 940 nm spectral band where water seems to share same profile but for most of the time its concentration are treated as constant background signals [Beckers (2013)]. Further, for our independent verification purposes, we have prepared 10% glucose (dextrose)-distill water solution and performed glucose absorption spectrum analysis to monitor absorption peaks within 300 nm to 1050 nm light wavelength by using Mini-spectrometer (AvaSpec-ULS2048-USB2-VA-50) of Avantes Inc.,USA.

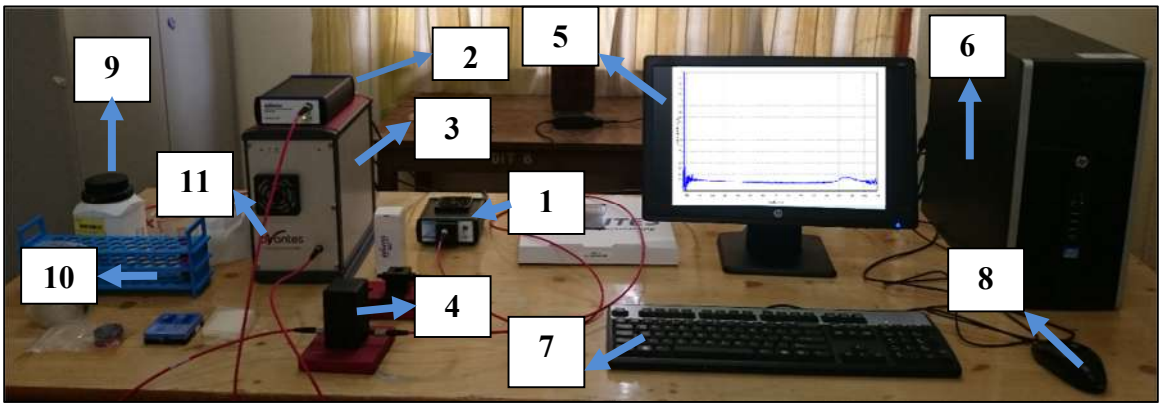

Figure 3.5: Mini-spectrometer of Avantes Inc.,USA;

1: Light source; **2:** Ultraviolet-Visible range spectrometer; **3:** Infrared range Spectrometer; **4:** Sample holder with cover and stand; **5:** Spectral reading program in computer display; **6:** Central processing unit; **7:** Keyboard; **8:** Computer mouse **9:** Dextrose powder bottle; **10:** Test tube stand; **11:** Optical fibre.

The figure 3.5 depicts the complete instrumental setup of Mini-spectrometer of Avantes Inc.,USA utilized in this present study. The figure 3.6 depicts the absorption

profile of 2ml 10% glucose in distill water solution. The figure 3.6 depicts that 10% Dextrose (glucose)-distill water solution exhibits absorption peaks near to 940 nm.

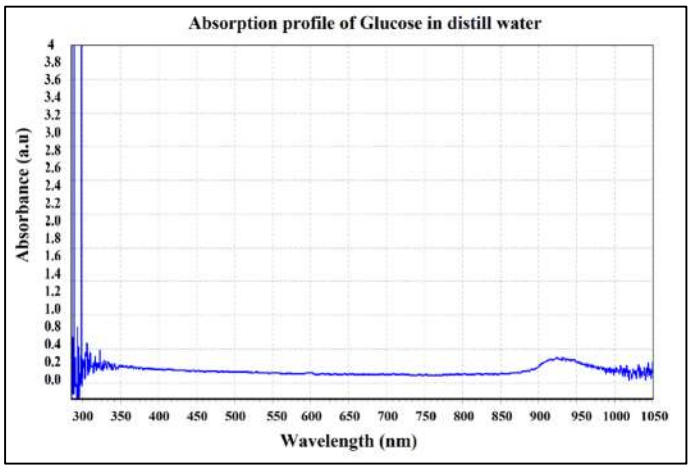

Figure 3.6: Absorption profile of 10% Dextrose (glucose)-distill water within 300 nm to 1050 nm.

Hence, considering wavelength such as 940 nm where water, oxyhemoglobin, reduced hemoglobin and other major intracellular absorbers exhibits low absorption profiles and good absorption profile from glucose molecules will be better to avoid any kind of particular noise interferences [Tuchin (2009); Kulkarni *et al.* (2010)]. Further, various researchers have utilized 940 nm for noninvasive glucose detection techniques. Some prominent researches in this field using 940 nm IR LED are as follows:

Bin *et al.* (2013) performed noninvasive blood glucose determinations utilizing 940 nm and 950 nm wavelength respectively. They have reported increase in linear voltage output with increase in glucose concentration for both of their in-vivo and in-vitro studies respectively. Vashist (2013) and Cohen *et al.* (2003) in their extensive research documents revealed that Sugar Track have utilized 940 nm (among other LEDs wavelengths) NIR wavelength for noninvasive glucose measurements respectively. Pande *et al.* (2013) performed noninvasive optical blood glucose measurement utilizing 940 nm as a particular wavelength and have documented good correlation between actual blood glucose levels and DSO (Digital Storage Oscilloscopes) based output voltages over more than eight patients respectively. Iiya-fine (2009) documented utilization of 940 nm wavelength as the reference LED wavelength in their respective glucose concentration

correlation based experimentations. Tirtariyadi (2009) utilized several light sources including 940 nm based LEDs for developing optical glucometer interface as a part of designing data collecting system for Near-Infrared bio-sensing applications. Cho *et al.* (2004) utilized different wavelength spectroscopy including 950 nm (very near to 940 nm) for noninvasive glucose measurement. They performed a different technique known as metabolic heat conformation methods and showed good results. Yeh *et al.* (2003) documented noninvasive glucose measurement technique utilizing glucose concentration effects over skin thermo optical responses. They have incorporated several LEDs for their experimental approaches including 935 nm (very near to 940 nm) and showed promising results. Kulkarni *et al.* (2010) documented noninvasive glucose determination by Photo Acoustic Spectroscopy utilizing 905 nm laser diode (near to 940 nm) and showed preliminary in vivo based good results. Yadav *et al.* (2014) designed Near Infrared LED based noninvasive glucose biosensor utilizing 940 nm due to its specific sensitivity for glucose molecules in the NIR domain. Their findings are promising and proved the potentiality of the 940 nm NIR spectra in measuring blood glucose levels through noninvasive techniques. Further, for significant wavelength selection we have performed glucose specificity and sensitivity analysis in this present work.

3.3 In-vitro analysis:

In this present work, in-vitro analysis evaluates the glucose specificity and sensitivity aspects. The specificity refers to the particular light wavelength where glucose exhibits maximum absorption peak characteristics. Similarly, the sensitivity refers to the ability of the particular light wavelength to respond in accordance with the effective variations in the glucose concentration levels.

3.3.1 Glucose molecule specificity analysis:

To determine the maximum wavelength specificity of glucose in distill water between 900 nm to 980 nm wavelength domain, we have prepared a stock solution of 2500 mg dextrose (glucose) per 10 ml of distill water. From that prepared concentration (w/v) stock solution, 2 ml of glucose in distill water solution has been pipette out, poured inside the cuvette. The figure 3.7 (a) depicts the Digital Spectrometer Model 305 of M.S Electronics Pvt. Ltd. (India) that is used in this present work to measure Absorbance (au = arbitrary unit) of glucose dissolved in distill water solution. The figure 3.7 (b) depicts

the absorption spectra of the glucose dissolved in distill water. The figure 3.7 (b) reveals that at 940 nm the glucose in distill water exhibits maximum absorption peak characteristics within Near Infrared spectral domain of 900 nm to 980 nm respectively.

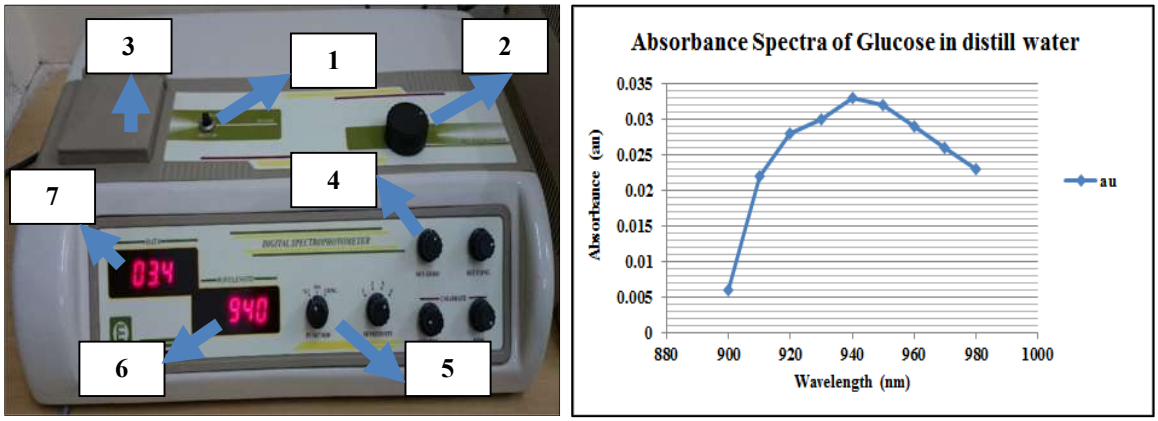

(a) **(b)**

Figure 3.7 (a): Digital spectrophotometer of M.S Electronics Pvt. Ltd. (India);

1: Wavelength range (UV or Visible) selection panel; **2:** Wavelength selection knob; **3:** Sample holder with cover lids; **4:** Coarse adjustment knobs; **5:** Absorption and Transmittance selection modes; **6:** Wavelength display; **7:** Result display.

(b): Absorption spectra of glucose in distill water between 900 nm to 980 nm.

Further, from Table 3.1, it can be depicted that glucose molecule exhibits absorption peak characteristics at 939 nm (very close to 940 nm) due to possible stretch and vibration of the second OH overtone band [Khalil (1999)] in its molecular structure.

3.3.2 Glucose molecule sensitivity analysis at 940 nm:

To determine the 940 nm wavelength degree of sensitivity for respective change in glucose concentration, we have prepared three sample concentration (w/v) solutions (dextrose in distill water) like 2500 mg/10 ml, 5000 mg/10 ml and 7500 mg/10 ml respectively.

Table 3.2: Glucose sensitivity analysis at 940 nm wavelength

Wavelength (nm)	2 ml from the prepared sample solutions (w/v)	Absorbance (au)	Concentration (ppm)
940	2500 mg/10 ml	0.033	071
	5000 mg/10 ml	0.045	113
	7500 mg/10 ml	0.067	150

The Digital Spectrometer Model 305 of M.S Electronics Pvt. Ltd. (India) performs the measurement analysis. The Table 3.2 depicts the output data from those 03 prepared sample concentration (w/v) solutions for glucose sensitivity analysis at 940 nm wavelength. The output data in Absorbance (arbitrary unit = au) and Concentration (parts per million = ppm) presents that 940 nm wavelength has been sensitive in detecting respective variations in glucose concentration (w/v) in the prepared sample solutions.

Hence, various factors like (i) "Optical Window" range (700-1100) nm; (ii) Typical peak characteristic of the glucose molecule at 940 nm; (iii) Acceptable specificity cum sensitivity for glucose at 940 nm; (iv) low cost and easy commercial availability; (v) Several literature reviews as mentioned above; favoring 940 nm for noninvasive blood glucose measurement strongly influenced us for this particular wavelength selection.

3.4 Amplitude Modulation (AM) concept and its application in our work:

In Modulation technique, the modulating signal modifies the other high frequency signal (typically sine wave) commonly known as the carrier signal. The three different types of Modulation techniques are Amplitude Modulation (AM); Frequency Modulation (FM); Phase Modulation (PM) [Frenzel *et al.* (2008)]. In (AM) Amplitude Modulation technique, the sine wave modulating signal modifies the amplitude of the sine wave carrier signal. Further, the carrier wave based instantaneous amplitude value varies in correlation with the amplitude and frequency changes of the modulating signal. The figure 3.8 depicts the sine wave modulating signal modulates a high frequency sine wave carrier signal. The frequency of the carrier wave is same during modulation phenomenon, but its amplitude changes in correlation with the modulating signal. Any variation in amplitude of the modulating signal (increase or decrease) causes correlated variation in both the amplitude peaks (positive or negative peaks) of the carrier wave [Frenzel *et al.* (2008)]. In figure 3.9, the imaginary line sketch joining both the positive and negative peaks of the carrier signal waveform provides the accurate form of the modulating signal. The imaginary line sketch on the carrier signal is termed as the envelope [Frenzel *et al.* (2008)]. Utilizing the functions of Trigonometry, the sine wave carrier signal mathematically expressed as:

$$v_c = V_c \sin 2\pi f_c t \qquad \text{Equation (4)}$$

In this equation (4), the v_c depicts the sine wave carrier signal instantaneous voltage value at a particular point of time in the cycle. The V_c depicts the constant unmodulated sine wave carrier signal peak value as calculated between minimum and maximum amplitude of anyone positive or negative going waveform waverings (Figure 3.9). The f_c represents the carrier sine wave frequency; and t represent a specific position in time throughout the carrier signal cycle [Frenzel *et al.* (2008)].

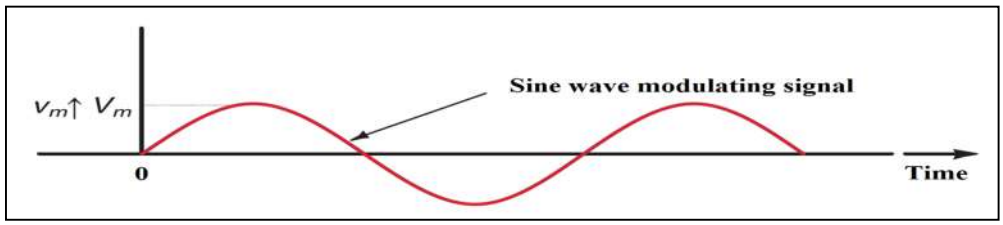

Figure 3.8: The sine wave modulating signal [Frenzel *et al.* (2008)]

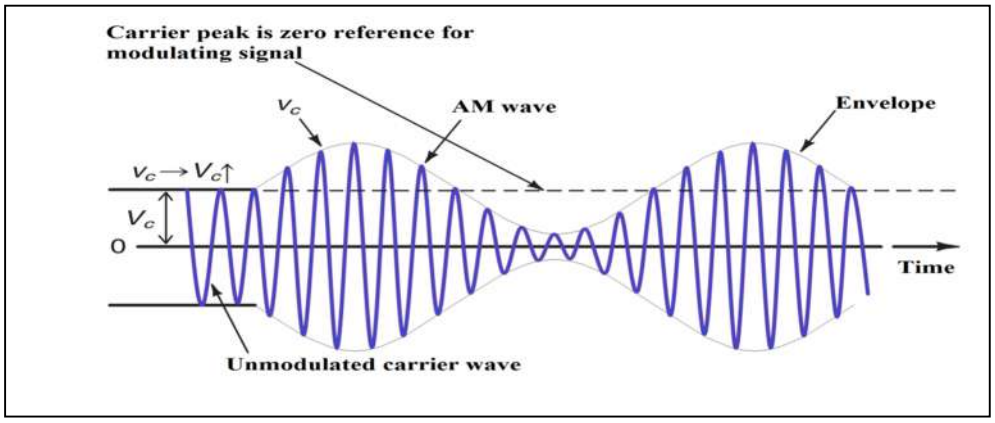

Figure 3.9: The modulated carrier wave signal [Frenzel *et al.* (2008)].

Utilizing the same functions of Trigonometry, the sine wave modulating signal mathematically expressed as:

$$v_m = V_m \sin 2\pi f_m t \qquad \text{Equation (5)}$$

Where, v_m = instantaneous value of the sine wave modulating signal.

V_m= peak amplitude of the sine wave modulating signal.

f_m = frequency of the sine wave modulating signal.

and t represent a specific position in time throughout the carrier signal cycle.

The figure 3.10 depicts that the modulating signal rather than zero as its reference position utilize the peak value of the carrier signal. The modulating signal envelope changes above and below the peak amplitude of the carrier signal. This fact presents that the modulating signal zero reference line overlaps with the peak value of the unmodulated carrier signal. Due to this phenomenon, the proportional amplitudes of the carrier and modulating signal are significant.

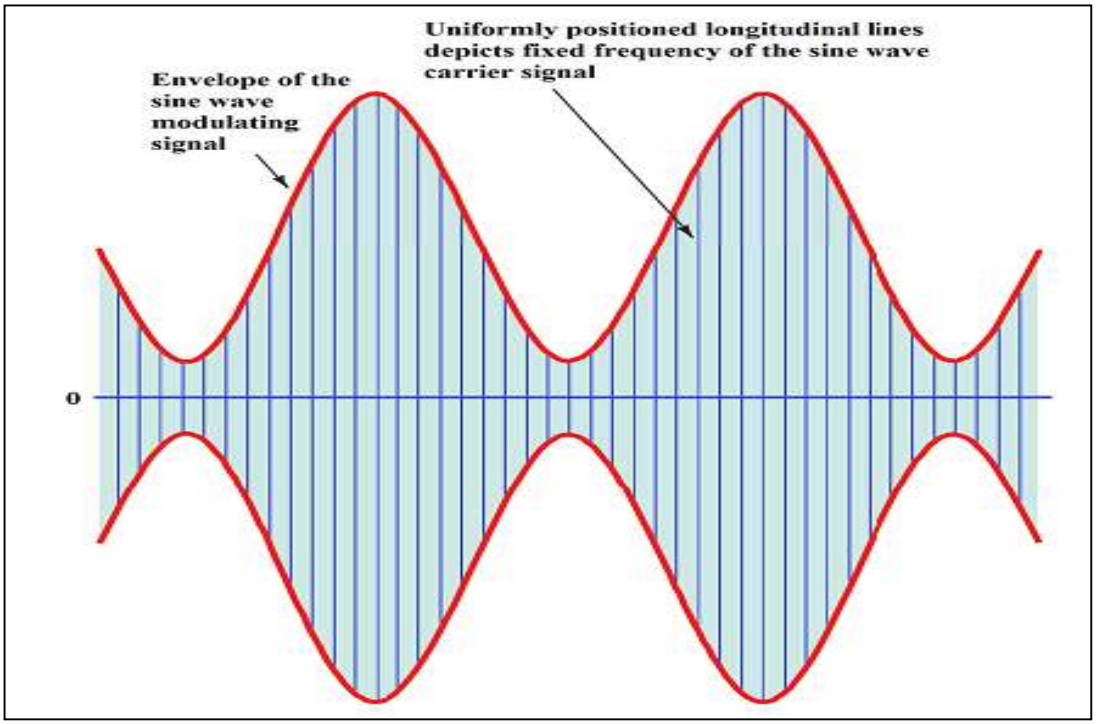

Figure 3.10: Simple depiction of Amplitude Modulated sine wave [Frenzel *et al.* (2008)].

Usually, the amplitude of the carrier signal must be greater than the amplitude of the modulating signal. In situations, where the amplitude of the modulating signal has been higher than the amplitude of the carrier signal, the distortion happens and erroneous data transmission occurs. In AM (Amplitude Modulation), it is specifically significant that the peak amplitude value of the modulating signal be lower than the peak amplitude value of the carrier signal. Mathematically represented as [Frenzel *et al.* (2008)]:

$$V_m < V_c \qquad \text{Equation (6)}$$

Now, the correlation called, as the modulation index (m) or modulating factor or coefficient or the degree of modulation, is the ratio and mathematically expressed as:

$$m = \frac{V_m}{V_C} \quad \text{Equation (7)}$$

V_m and V_C represents the peak values of both the signals and carrier voltage is the unmodulated value. Multiplying the modulation index (m) with 100 yields modulation percentage. The values of both the carrier and modulating wave signals contributes to yield the mathematical expression for complete modulated wave signal. The carrier peak value is the reference point for the modulating signal. To measure the instantaneous value of either the top or bottom voltage envelope v_1, the mathematical equation is [Frenzel *et al.* (2008)]:

$$v_1 = V_c + v_m = V_c + V_m \sin 2\pi f_m t \quad \text{Equation (8)}$$

This equation (8) represents the fact that the modulating signal instantaneous value algebraically sums to the carrier peak value. Hence, we represent the instantaneous value of the complete modulated wave (v_2) by replacing (v_1) for the carrier signal voltage (V_c) peak value as follows [Frenzel *et al.* (2008)]:

$$v_2 = v_1 \sin 2\pi f_c t \quad \text{Equation (9)}$$

The expression for v_1 in equation (8), utilized to express v_1 in equation (9) and by expanding, we get:

$$v_2 = (V_c + V_m \sin 2\pi f_m t) \sin 2\pi f_c t \quad \text{Equation (10)}$$

$$= V_c \sin 2\pi f_c t + (V_m \sin 2\pi f_m t)(\sin 2\pi f_c t) \quad \text{Equation (11)}$$

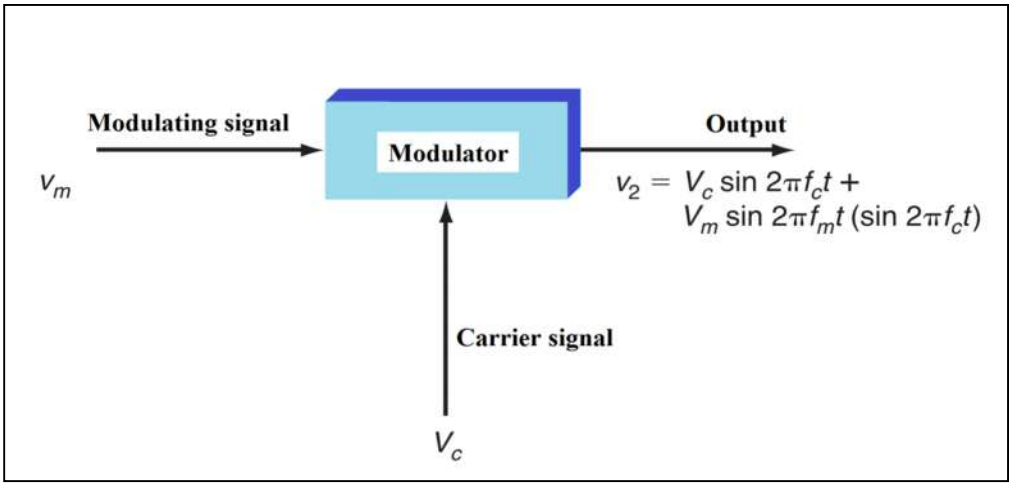

Figure 3.11: Amplitude Modulator with input and output signals [Frenzel *et al.* (2008)].

Where, v_2 stands for the AM wave instantaneous value ($or\ v_{AM}$); $V_c \sin 2\pi f_c t$ represent the modulating wave signal, and $(V_m \sin 2\pi f_m t)(\sin 2\pi f_c t)$ depicts the carrier signal multiplied by the modulating signal [Frenzel *et al.* (2008)]. The part that produces AM (Amplitude Modulation) is termed as the modulator unit. The modulator has two inputs, the carrier wave signal, and the modulating wave signal. The figure 3.11 depicts the resulting modulated output signal. The second part of the expression represents the main characteristic of the Amplitude Modulation. For AM to occur, the modulator unit must be able to perform the mathematical multiplication of the carrier and the modulating signals. Hence, the AM waves are the product of the carrier and the modulating signals [Frenzel *et al.* (2008)]. In this present work, the Amplitude Modulated signal serves as an input signal to the Ultra-Sound Transmitter (UST) unit for generating Amplitude Modulated ultrasonic radiating waves towards the measurement site (fingertip).

3.5. Fabricated prototype descriptions:

The figure 3.12 presents the block diagram of our noninvasive technique based prototype (MUS-IR) unit for measuring blood glucose levels in the study subjects.

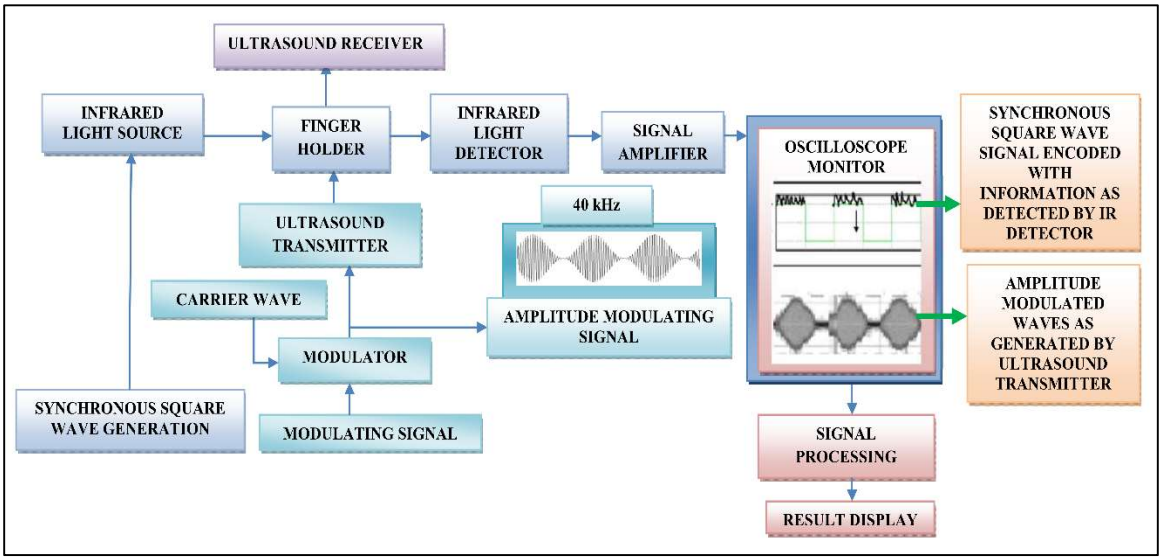

Figure 3.12: Block diagram of noninvasive technique based prototype (MUS-IR) unit.

Our method utilizes modulated ultrasound and infrared light based optical technique for noninvasive measurement of blood glucose levels. The modulating signal unit provides modulating sine wave signals. The Carrier wave unit provides carrier wave

signals. Both this signals serves as an input to the modulator unit. The modulator unit produces amplitude modulated sine wave signals to the ultrasound transmitter unit. The Ultrasound transmitter unit produces ultrasonic amplitude modulated sine waves to the finger holder unit.

The amplitude modulated ultrasonic waves excites the fingertip portion, as a result different constituent molecules vibrates at their specific response frequency depending upon their weight, shape, size, and properties of the medium in which they are present [Chowdhury *et al.* (2015); Radel *et al.* (2010); Coakley (1997)].

The ultrasound receiver unit cross checks the pattern of amplitude-modulated signal waves as generated by ultrasound transmitter unit as shown in the oscilloscope monitor block in figure 3.12 respectively. The synchronous square wave generations are provided to the Infrared light source unit, to deliver square wave pulses to the finger holder unit. Further, the specific vibrations produced due to amplitude modulated ultrasonic waves are detected using the infrared light and detector unit. The amplified output response signal is in the form of synchronous square wave signals as shown in the oscilloscope monitor block of figure 3.12, which carries encoded information about the concentration of different constituent molecules. This modulated light response signal as collected using Infrared light detector are suitably processed to extract the information of about the blood glucose concentration and then the display unit shows the results.

The descriptions of its main functional parts are as follows:

3.5.1 Modulating signal:

In this present work, for modulating signal generation, we have utilized the sine wave output from the signal generator unit of the Model EDC-20 of Edkits Electronics, India. The Table 3.3 depicts the signal generator unit features and benefits.

Table 3.3: Model EDC-20 of Edkits Electronics (Sine wave signal generator)

Features and benefits	
Signal Generator	1 Hz to 100 kHz with 0 to 12 V peak to peaks for Sine Wave
Frequency Response	+/- 0.5 db over the entire range
Power Input	230 V + 10 % 50 Hz

The figure 3.13 represents the typical pattern of the modulating sine waveform generated here and displayed on the monitor of DSO (Digital Storage Oscilloscope - Nvis 102 CT Digital Storage Oscilloscope of 25 MHz, 50MSa/s) based upon voltage and current variations with respect to the time domain.

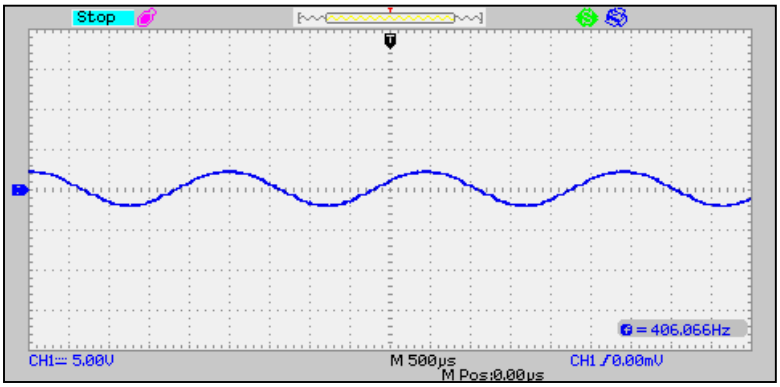

Figure 3.13: Modulating sine wave signal

The Table 3.4 depicts the generated modulated sine waveform various characteristics and its descriptions are as follows:

Table 3.4: Modulating sine wave signal characteristics

Modulating sine wave signal characteristics	
CH1	5.00 V
Frequency (f)	406.06 Hz
V_{pp}	4.40 V
V_{rms}	1.40 V
+duty	50.0 %
-duty	49.0 %
+wid	1.24 ms
-wid	1.22 ms

CH1 stands for the channel-1 symbol. The CH1 of DSO represents this signal channel with 5.00 V (Volt) as its vertical scaling factor. f = 406.06 Hz represents the modulating sine wave signal frequency. The V_{pp} = 4.40 V signifies the measurement of

the absolute difference between the maximum and minimum peaks of the entire waveform. V_{rms} = 1.40 V denotes the true Root Mean Square voltage over the entire waveform. +duty = 50% indicates the first cycle waveform measurement. Positive Duty Cycle is the ratio between positive pulse width and period. –duty= 49% indicates the first cycle waveform measurement. Negative Duty Cycle is the ratio between negative pulse width and period. Further, the +Width = 1.24 ms indicates the time between the first rising edge and the next falling edge at the waveform 50% level. -Width = 1.22 ms indicates the time between the first falling edge and the next rising edge at the waveform 50% level.

This modulated sine waveform functions as an input modulating signal (along with the input carrier signal) to AD633 to produce amplitude-modulated waves towards the UST unit in our noninvasive technique based prototype (MUS-IR) unit.

3.5.2 Carrier wave:

The Testronix Model-72 is a sine-square oscillator and capable of providing sine/square wave or both the signals simultaneously. In this present work, the sine wave oscillator output unit of Testronix Model-72 (India) produces carrier sine wave (40 kHz frequency) signal required for generating amplitude modulation in our noninvasive technique based prototype (MUS-IR) unit. Further, the Table 3.5 depicts the features and benefits of Testronix Model-72 (sine-square Oscillator).

Table 3.5: Testronix Model-72 (Sine-Square Oscillator)

Features and benefits	
Frequency	1 Hz to 1 MHz in 6 decades continuously variable
Output Amplitude	Continuously variable up to 30 volts (peak - peak) with 3 decade selection and continuously variable amplitude control
Frequency Response	+/- 0.5 db over the entire range
Power Input	230 V + 10 % 50 Hz.

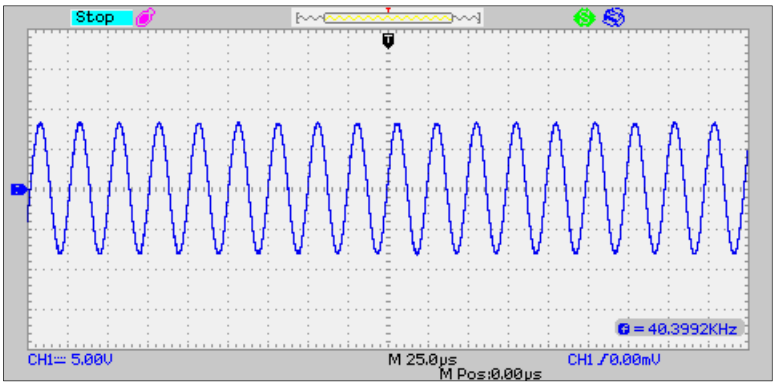

Figure 3.14: Carrier sine wave signal

Table 3.6: Carrier sine wave signal characteristics

Carrier sine wave signal characteristics	
CH1	5.00 V
Frequency (f)	40.39 kHz
V_{pp}	16.60 V
V_{rms}	5.60 V
+duty	50.0 %
-duty	49.0 %
+wid	12.56 µs
-wid	12.20 µs

The signal illustrated in figure 3.14 depicts the change in the carrier amplitude with respect to the time domain. The Table 3.6 presents the voltage and current variation based measurements that occur in the time domain based signals as displayed on monitor of the DSO. It represents in this present work, the CH1 (Channel 1 of DSO) has been selected for this signal analysis. The frequency (f) of the carrier sine wave signal has been 40.39 kHz. The V_{pp} and V_{rms} measured values are 16.60 V and 5.60 V respectively. Its +duty and -duty cycles has been 50% and 49% respectively. Further, its +width and -width has been 12.56 µs and 12.20 µs respectively. This carrier sine waveform functions as an input carrier signal (along with the input-modulating signal) to AD633 to produce amplitude-modulated waves towards the UST unit in our noninvasive technique based prototype (MUS-IR) unit.

3.5.3 Modulator unit:

The modulator unit produces amplitude-modulated signals to the UST (Ultrasonic Transmitter) Unit. Both the modulating and carrier signals serves as an input signals to it. In our prototype (MUS-IR) unit, the AD633 acts as a signal modulator unit, which is capable of producing an amplitude modulating signal of interest. The Table 3.7 depicts the features and benefits of the low cost analog multiplier AD633 [AD633 Data Sheet, Analog Devices, Inc., 1999] utilized in the present work as the modulator circuit unit.

Table 3.7: AD633 features and benefits [AD633 Data Sheet, Analog Devices, Inc., 1999]

AD633	
Features and benefits	It has four quadrant and act as an analog multiplier.
	Negligible over loading of source signals due to high input resistances of 10 MΩ.
	Buried Zener provides internal voltage scaling, full-scale low impedance voltage output.
	Multiplier accuracy is independent of supply characteristics.
	Power supply needed between ±8 V to ±18 V.
	Cost efficient, easy to use, stable, and reliable.

3.5.3.1 Functional descriptions:

The AD633 is an economical analog multiplier consists of (i) inbuilt trans-linear core (ii) buried Zener as reference, (ii) unity gain attached output amplifier (iii) summing node availability. The figure 3.15 depicts the functional block diagram. The voltage to current converters converts the differential X and Y inputs in to differential currents. The multiplying core generates the product of these currents. The buried Zener as reference delivers total scaling of 10 V. The sum of $\left[\frac{(X \times Y)}{10} + Z\right]$ is provided to the output amplifier. The summing node Z permits addition of two or more outputs, performs conversion of voltage to current, and executes analog operational functions [AD633 Data Sheet, Analog Devices, Inc., 1999].

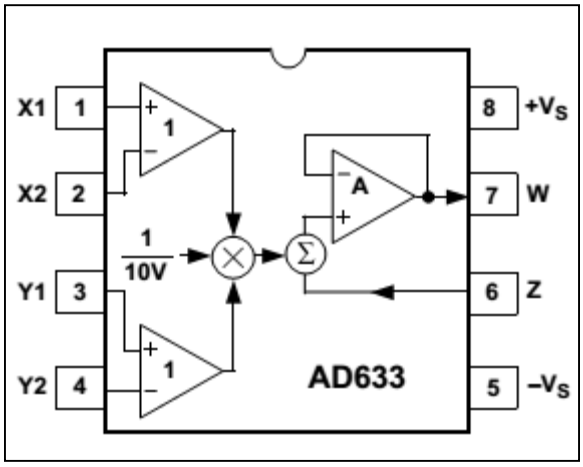

Figure 3.15: Functional block diagram of AD633 [AD633 Data Sheet, Analog Devices, Inc., 1999]

Assessment of the functional block diagram depicts the transfer function to be:

$$W = \frac{(X_1 - X_2)(Y_1 - Y_2)}{10V} + Z \qquad \text{Equation (12)}$$

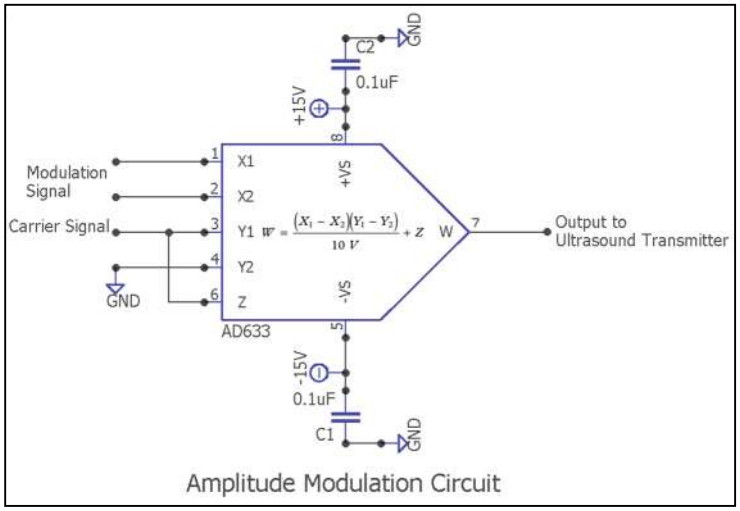

Figure 3.16: Amplitude Modulation circuit for providing modulation input to the Ultrasound Transmitter unit.

In this present work, the carrier signal and modulating signal act as the input signal to IC AD633 respectively. The power supply of ±15 V drives the modulator unit (AD633). The figure 3.16 depicts the circuit diagram of AD633 as the linear amplitude modulator. The AD633 multiples both the carrier and modulating signals inputs and

produces double sideband signals. Further, the carrier wave signal carried frontward to the Z input point in AD633 chip to sum with that double side band signals. After that, it yields double-sideband with carrier output signals. To measure the resonance frequency, finely controlling the frequency dial of the signal generators (modulating and carrier waves) produces desired voltage sketch on the DSO monitor. Tuning of modulation index largely depends up on the variation of the amplitude modulation [Se-yuen (2003)].

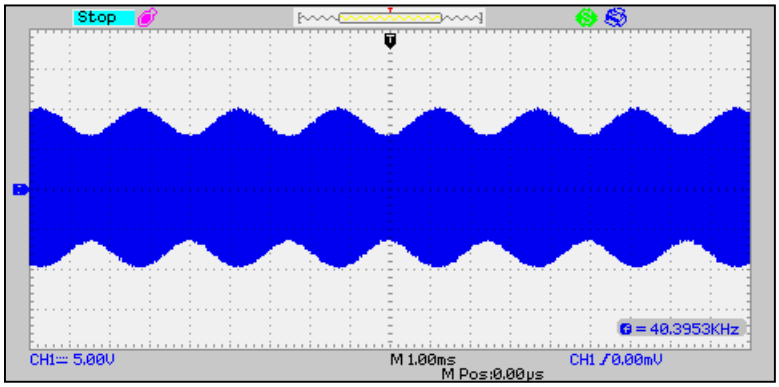

Figure 3.17: Amplitude Modulated signal waveform

Table 3.8: Amplitude Modulated Signal characteristics

Amplitude Modulated Signal characteristics	
CH1	5.00 V
Frequency (f)	40.39 kHz
V_{pp}	20.00 V
V_{rms}	5.80 V
+duty	50.0 %
-duty	50.0 %
+wid	12.00 µs
-wid	12.00 µs

The figure 3.17 and Table 3.8 represents the amplitude modulated signal waveform characteristics as generated from the AD633 unit. The generated signal waveform parameters based on current and voltage variations with respect to time domain as measured by the DSO unit are depicted in Table 3.8 respectively. It represents

in this present work, the CH1 (Channel 1 of DSO) has been selected for this signal analysis. The frequency (f) of the Amplitude-Modulated (AM) signal has been 40.39 kHz. The V_{pp} and V_{rms} measured values are 20.00 V and 5.80 V respectively. Its +duty and -duty cycles has been 50% and 50% respectively. Further, its +width and –width has been 12.00 µs and 12.00 µs respectively.

Further, this signal serves as an input to the Ultrasound Transmitter Unit to generate amplitude modulated ultrasonic signal waves required for producing vibration inside the measurement site.

3.5.4 Ultra Sound Transmitter (UST) and Ultra Sound Receiver (USR) units:

We have selected Ultrasound Transmitter and Receiver of 40 kHz central frequency. The 40 kHz ultrasonic frequency is medically safe for its application over human beings [Se-yuen (2003)].The features and benefits of UST and USR units as provide by the manufacturer are:

Both the UST and USR transducer operates at the central frequency of 40±1.0 kHz respectively. Commercially, both of it comes in matched pairs with white or black mesh in aluminum casings. Transmitter can withstand input voltage of 20 V_{rms} maximum and produces sound pressure level of 110 ± 5 dB (approximately) at 10 V and 30 cm respectively. It has been documented that same unit can be utilized as the Transmitter or the Receiver as well. However, Transmitter (T) and Receiver (R) units have been marked with ‘T’ and ‘R’ behind its respective aluminum casings. The Receiver possess the mesh diameter of 7.5 m and its effective sensing zone is about 20 mm^2 respectively.

The voltage calculation through the series of low resistance resistors yields that, when the input voltage (V_{input}) is 10 V and, the input current (I_{input}) through the Transmitter is nearly 20 mA at resonance. Therefore, the minimum power needed for signal production is $\frac{1}{2}V_{input}.I_{input} \approx 100\ mW$ respectively. The amplitude-modulated waves as generated from the respective modulator unit serves as signal input to the UST unit. Consequently, the UST functional unit produces output signal in the form of ultrasonic amplitude modulated waves towards the finger holder unit. The figure 3.18 depicts the schematic of this phenomenon.

To measure the output wave characteristics for direct transmission, both the UST and USR units positioned in a straight line over the optical bench facing each other.

Herein, the optical bench acts as the Lloyd's mirror, producing a pressure antinode within the length of transmission line over the optical bench surface [Se-yuen (2003)]. In order to minimize the unwanted reflections, all the instruments (Signal Generator, DSO) is positioned at a distance of 50 cm away from the sound propagation path length. Further, for preventing 50 Hz noise originating from the mains, a shunt resistor (10 kohm) mounted across the USR leads. Generally, in mechanical defect free USR units, the maximum resonance occurs particularly at 40 kHz frequency.

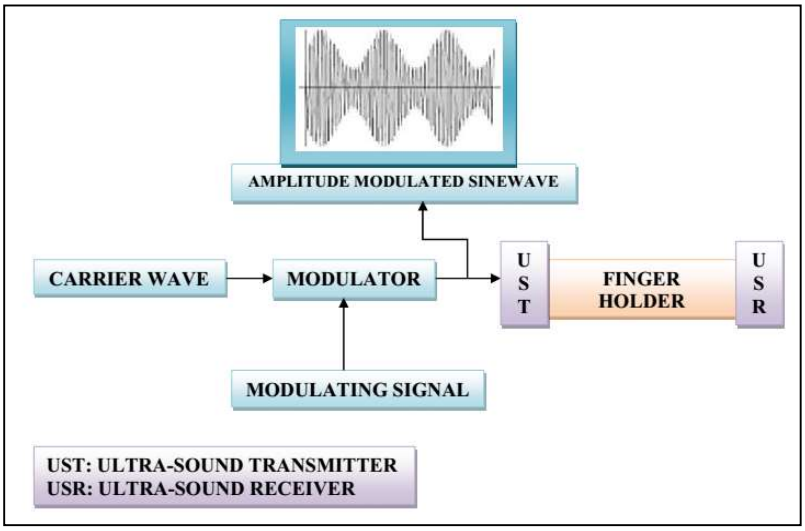

Figure 3.18: Amplitude Modulated waveform pattern as provided to the finger holder.

The figure 3.19 and Table 3.9 depicts the output waveform typical figure and its characteristics as measured from the USR unit at resonance by the DSO.

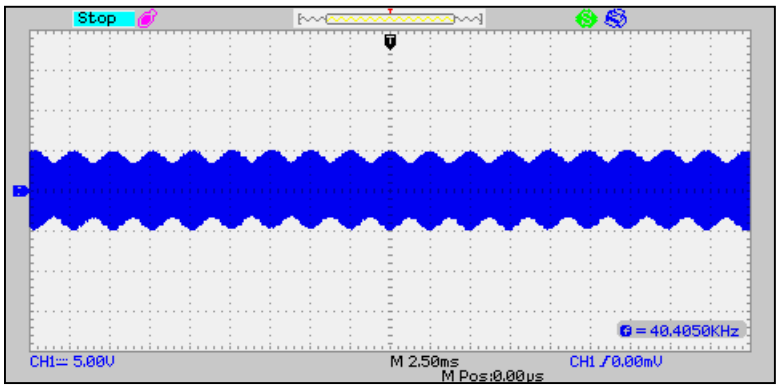

Figure 3.19: The output waveform pattern from the USR unit as recorded by DSO

It represents in this present work, the CH1 (Channel 1 of DSO) has been selected for this signal analysis. The frequency (f) of the output waveform signal has been 40.40 kHz. The V_{pp} and V_{rms} measured values are 10.00 V and 2.80 V respectively. Its +duty and -duty cycles has been 50% and 50% respectively. Further, its +width and –width has been 36.00 µs and 36.00 µs respectively.

Table 3.9: Waveform features as received by the USR unit

Waveform parameters	
CH1	5.00 V
Frequency (f)	40.40 kHz
V_{pp}	10.00 V
V_{rms}	2.80 V
+duty	50.0 %
-duty	50.0 %
+wid	36.00 µs
-wid	36.00 µs

In this present work, the USR unit checks the amplitude modulation quality of ultrasonic waves generated from the UST unit towards the finger holder unit. As modulating, the ultrasonic waves produce high SNR (Signal to Noise Ratio) for a chosen group of frequencies with respect to the Modulation function [Urban *et al.* (2010)].

3.5.5 Finger holder unit (Finger probe):

Finger holder probe upholds the human finger in precise geometrical position required for accurate ultrasonic wave propagation and IR light transmission purposes respectively.

Figure 3.20: Finger holder probe of our noninvasive technique based prototype unit.

The finger holder probe in figure 3.20 helps in steady positioning of Ultrasonic and IR light units, with respect to the finger positioning during signal acquisition periods.

Further, it minimizes the unwanted errors such as motion related artifacts, wrong finger positioning, background light interferences.

3.5.6 Synchronous square wave generator:

In this present work, we have selected the function generator (3 MHz, HM-5030-4) of Scientific Pvt. Ltd (India) for square wave generation.

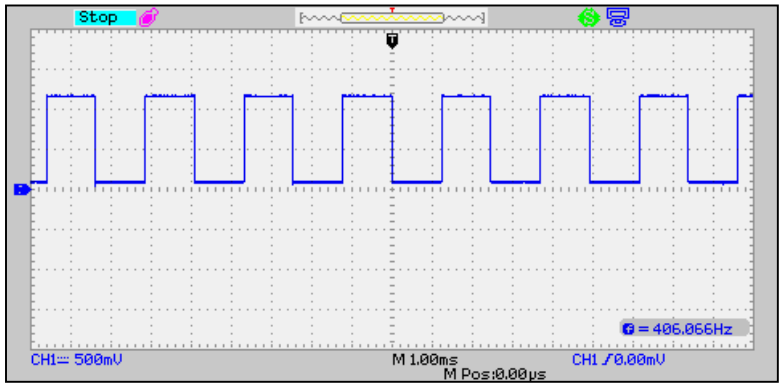

Figure 3.21: Square wave signal

This unit serves an input signal to drive the IR LED of 940 nm. In order to match the heart cycle based pulsatile motion of the blood flow, the application of the square wave is an essential prerequisite [Tuchin (2009)]. The figure 3.21 and Table 3.10 depicts the square wave input signal and its characteristics as measured by the DSO.

Table 3.10: Square wave signal characteristics

Waveform characteristics	
CH1	500 mV
Frequency (f)	406.06 Hz
V_{pp}	1.18 V
V_{rms}	820.0 mV
+duty	50.0 %
-duty	49.0 %
+wid	1.24 ms
-wid	1.22 ms

The Table 3.10 represents in this present work, the CH1 (Channel 1 of DSO) has been selected for this signal analysis. The frequency (f) of the square wave signal has been 406.06 Hz. The V_{pp} and V_{rms} measured values are 1.18 V and 820.0 mV respectively. Its +duty and -duty cycles has been 50% and 49% respectively. Further, its +width and –width has been 1.24 ms and 1.24 ms respectively.

3.5.7 Infrared light source:

In this present work, we have utilized the 940 nm Infrared Light Emitting Diode (B5B-940-8) of Roithner LaserTechnik Vienna, Austria, for irradiating fingertip of the study subjects. The specifications as provided by the manufacturer are as follows: It is round type with 5 mm diameter. Lens color is water clear with flange. It emits infrared light through GaAlAs/GaAs technology with peak wavelength (λ_p) at 940 nm at $(I_F) = 50\ mA$ respectively. Its Power Dissipation and Peak forwarding current (1/10 Duty cycle @1 kHz) has been denoted as $(P_D) = 160\ mW$ and $(I_{FP}) = 1\ A$ respectively. It has Continuous Forwarding Current $(I_F)\ of\ 100\ mA$ and the Reverse Voltage $(V_R)\ of\ 5.0V$ respectively. Spectrum Radiation Bandwidth (δλ) of 50 nm, when $(I_F) = 50\ mA$. Radiated output power (P_o) of 32 to 48 mW, when $(I_F) = 50\ mA$. Forward voltage (V_F) of 1.0 to 1.6 V, when $(I_F) = 50\ mA$. Reverse Current (I_R) of 100 uA, when $(V_R) = 5\ V$. Operating Temperature Range (T_{OPR}) is between $-40 + 85\ ^0$C respectively [Data Sheet of B5B-940-8, Roithner LaserTechnik Vienna, Austria].

3.5.7.1 940 nm LED wavelength verification:

Infrared Light Emitting Diode (B5B-940-8) of Roithner LaserTechnik Vienna, Austria has been utilized here.

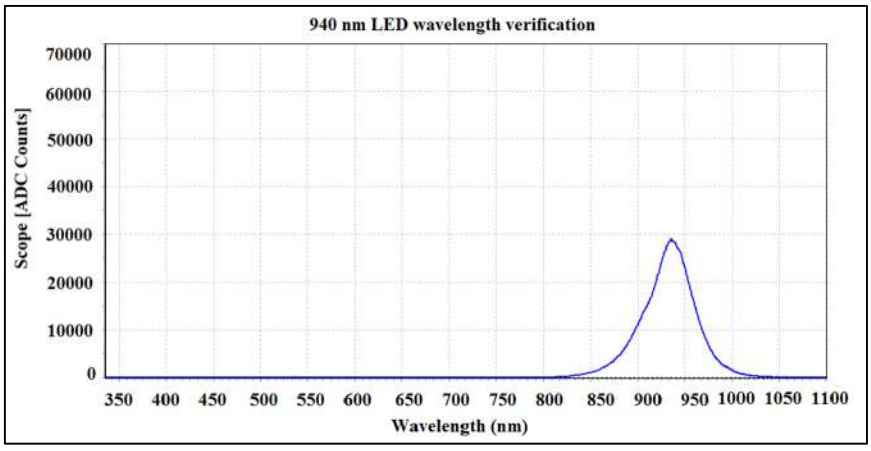

Figure 3.22: Typical spectral intensity distribution of the IR LED used in our prototype.

It has been cross validated for checking its typical maximum spectral intensity by utilizing Mini-spectrometer (AvaSpec-ULS2048-USB2-VA-50) of Avantes Inc.,USA. The figure 3.22 shows the good quality spectral intensity near to 940 nm that satisfies the essential requirement for our clinical study.

3.5.8 Infrared (IR) detector (Photodiode):

In this present work, we have utilized EPD-1300-5.3; InGaAs selective IR photodiode of Roithner LaserTechnik, Vienna, Austria, for capturing transmitted light from the infrared light (940 nm) irradiated human finger to measure noninvasive blood glucose levels. This photodiode is perfect for detection of pulsed light with sensitivity starting from 800 nm to 1750 nm. The figure 3.23 depicts the IR photodiode circuit diagram with power supply of 4.5 V. In reverse bias condition, the photodiode generates current, which is the function of the transmitted light power (p) and its wavelength. The degree of responsitivity $\Re$ (λ) provides the total value of photocurrent per transmitted light energy. The load resistor (R_L) placement between the anode of the photodiode and the circuit ground converts the photodiode current into the voltage. The voltage output (V_{output}) mathematically expressed as [Data Sheet of EPD-1300-5.3, Roithner LaserTechnik Vienna, Austria]:

$$V_{output} = p \times \Re \times R_L \qquad \text{Equation (13)}$$

The specifications as provided by the manufacturer are as follows:

The photodiode characteristic includes InGaAs technology with an active area of Φ = 300 µm. Mounted over a lead frame and encapsulated within a standard clear 5 mm epoxy package. The break down voltage (V_R) indicated to be = 5 V, when (I_R) = 10 µA. The Photodiode operating Temperature Range (T_{OPR}) is between $-40 + 85\ ^0$C.

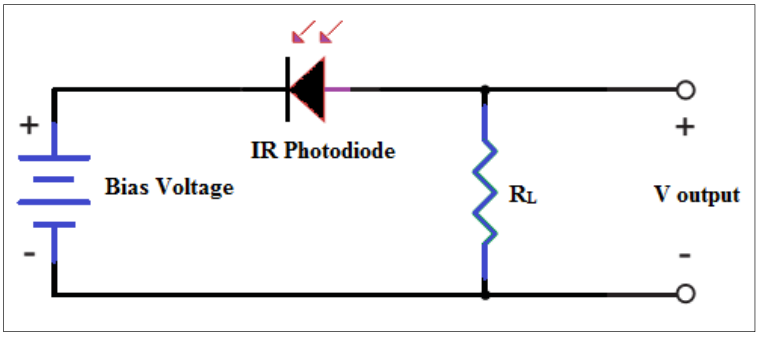

Figure 3.23: Infrared photodiode circuit diagram.

3.5.9 Signal processing unit:

In this present work, the signal processing toolbox of MATLAB performs observed signal analysis in FFT domain to extract blood glucose level related embedded information.

3.5.10 Result display:

This part of prototype unit displays the P-BGL (Predicted-Blood Glucose Level) in mg/dl.

3.6 In-vitro experiment:

In order to establish a noninvasive blood glucose measurement initially, (i) in-vitro experiments using aqueous solution of glucose and (ii) in-vitro quasi-finger system (optical tissue phantoms) based experiments are highly significant. Optical phantoms resemble tissue optical properties, in which various elementary principles, scientific concepts are tested [Amir *et al.* (2007); Kohl (1995)].

3.6.1 In-vitro experiment using glucose in distill water:

Our initial step includes glucose solution based in-vitro experiments to test the measurement principle of our modulated ultrasound and infrared light based technique. The glucose concentration range selected from 0 mg/dl to 500 mg/dl to cover both the physiological and pathological ranges. The Dextrose Injection I.P. 5% (D5) mixed with distilled water in different proportions (0; 50; 100; 150; 200; 250; 300; 350; 400; 450; and 500 mg/dl) to vary the glucose solution concentration from 0 mg/dl to 500 mg/dl. The next step includes placing each prepared samples (fixed 4 ml quantity) inside the sample holder of our prototype unit for its respective glucose concentration measurement. In the MUS-IR unit, the in-vitro sample holder unit have similar orientations like that of the finger holder unit. Further, the ultrasound transmitter is positioned on top of the sample holder to eliminate variations arising from sample holder-ultrasonic transducer interface between the measurements.

Finally, the output signals are stored for signal processing. The main observation is to monitor the changes of the peak amplitude values (mV) in the FFT domain with respect to change in glucose concentration solutions.

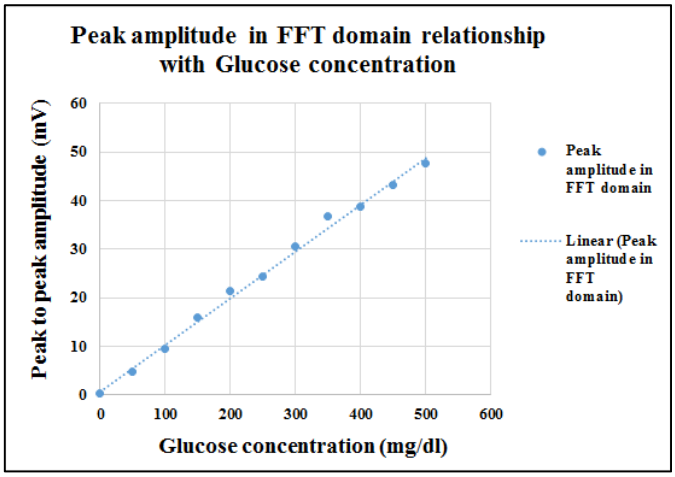

Figure 3.24: Peak-to-peak amplitude spectrum (in FFT domain) measured at 940 nm from solutions with changing glucose concentration.

3.6.1.1 Result analysis:

The figure 3.24 depicts that peak-to-peak amplitude in FFT domain increases with respective increase in glucose concentrations, from 0 mg/dl to 500 mg/dl respectively.

3.6.2 In-vitro experiment using quasi-finger system:

In this, present work, our approach include preparing the quasi-finger system to mimic finger absorption and scattering characteristics in the infrared spectral domain. The Intralipid phantom resembles tissue scattering aspects, while absorption is accounted here by direct addition of the prepared whole blood samples (fasting and postprandial) to it to from the quasi-finger system. Mixture of both these constituents resembles blood tissue medium. The constant level of oxygen in prepared samples is essential to obtain glucose concentration derived results [Amir *et al.* (2007); Kohl (1995)].

Herein, in-vitro (with this prepared quasi-finger system) phantom sample analysis performed, to explore the glucose sensitivity of our noninvasive technique based prototype unit.

3.6.2.1 Study subjects:

In total 12 adult subjects participated in this clinical study. Two subjects are healthy normal, three subjects had pre-diabetes, and seven subjects had diabetes. The mean ± standard deviations of age is 41±5 years and mean ± standard deviations of body mass index is 27.3±3 years. Overall, ten subjects were male and two subjects were

female. The clinical study reported here, is in accordance with the standard ethical procedures and performed with the informed consent of all the respective subjects. The clinical study was approved by the Ethical Committee Board of Faculty of Medicine, Institute of Medical Sciences, Banaras Hindu University; Varanasi, India.

3.6.2.2 Sample preparation:

The sample preparation steps include:

Step 1: Collection of whole blood samples from the study subjects in vacuum-based blood collecting vials, where K_2 EDTA (Ethylene Di-amine Tetra-acetic Acid) is present as an anticlotting agent. Addition of Phosphate Buffer Solution (PBS) to maintain the pH levels in the samples.

Step 2: De-oxygenation of the whole blood samples by nitrogen gas bubbling for 45 minutes to reduce oxygen influence over glucose measurement.

Step 3: 1 ml of the Intralipid suspension mixed with 1 ml of whole blood sample to form a quasi-finger system resembling blood tissue optical properties.

Step 4: Placing each prepared phantom samples inside the sample holder of our prototype unit for its respective glucose concentration measurement.

The invasive measurements performed to measure and compare the blood glucose levels with the FFT domain based peak amplitude (mV).

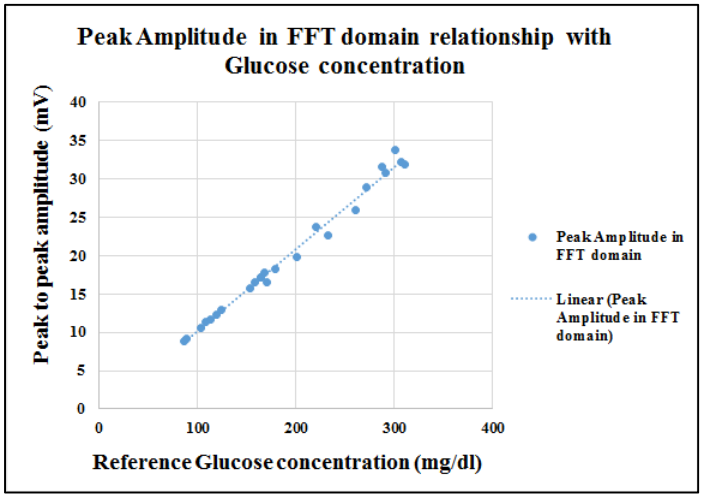

Figure 3.25: The peak-to-peak amplitude in FFT domain relationship with varying glucose concentration in fasting and 2 hour postprandial in-vitro samples.

3.6.2.3 Result analysis:

The figure 3.25 represents the peak amplitude in FFT domain during fasting and 2-hour postprandial stages and its effective correlation with the reference (invasive) blood glucose concentration-levels. The peak amplitude (mV) in FFT domain changes in correlation with the variation of reference (invasive) blood glucose levels.

These correlated changes indicate towards the sensitivity (at 940 nm) of our prototype unit in detecting glucose concentration variations in respective quasi-finger system based in-vitro samples.

Further, peak amplitude in FFT domain increases with increase in blood glucose levels, this phenomenon indicate towards the glucose concentration induced light clearing effects. As increase in glucose concentration in-vitro samples causes reduction of the scattering effects, which minimizes the mismatch of the refractive index acquiescently, increase in light transmission occurs [Amir *et al.* (2007); Kohl (1995)].

The experimental illustration of this phenomenon has been provided in Chapter 4 of this present thesis work.

The in-vitro experiments showed strong correlation between measured glucose levels and the actual concentration and hence this phenomenon forms the benchmark as well as foundation for performing in-vivo experiments to establish the performance and efficacy of our technique in noninvasive blood glucose measurement.

3.7 Preliminary in-vivo analysis:

A study subject (age = 26 years, height = 164 cm, weight = 74 kg, and, Random Blood Glucose Level = 85±5.0 mg/dl) inserts his index finger in the finger holder of our prototype unit. After that, the modulated ultrasound generates vibration in the measurement site. At the same time, the infrared light in synchronous square wave mode transmits through the fingertip to yield ultrasound modulated light response signal. Afterwards, the IR photodiode picks up the transmitted (from the human finger) IR light signals.

The clinical study reported here are in accordance with the standard ethical procedures and performed with the informed consent of the respective study subject. The Ethical committee of IMS-BHU, Varanasi approved the clinical study.

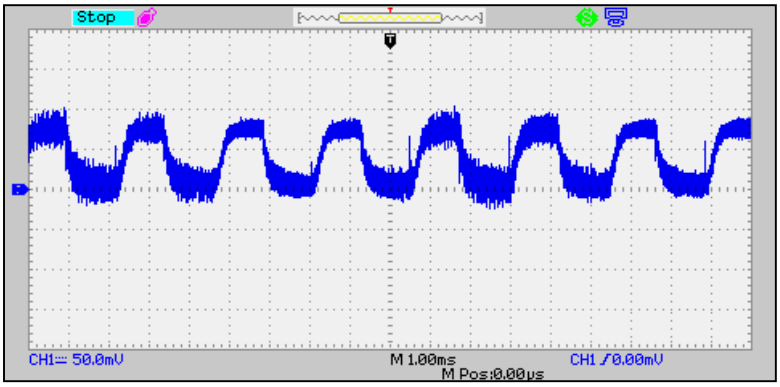

Figure 3.26: The typical output signal acquired from the fingertip of the study subject.

Table 3.11: The output signal parameters as acquired from the fingertip of the study subject

Waveform characteristics	
CH1	50 mV
V_{pp}	128.0 mV
V_{rms}	50.00 mV
+duty	50.0 %
-duty	49.0 %
+wid	1.43 ms
-wid	1.03 ms

The acquired signals are stored and analyzed for blood glucose concentration related information analysis. The figure 3.26 and Table 3.11 depicts the DSO based one of the typical output sample signal, and its various parameters, as detected by the infrared photodiode of our prototype unit from the measurement site of the study subject. At that same time, the study subject invasive blood glucose level has been 94 mg/dl. The Table 3.11 represents in this present work, the CH1 (Channel 1 of DSO) has been selected for this signal analysis. The V_{pp} and V_{rms} measured values are 128.0 mV and 50.0 mV respectively. Its +duty and -duty cycles has been 50% and 49% respectively. Further, its +width and –width has been 1.43 ms and 1.03 ms respectively. The figure 3.27 depicts the FFT of the typical in-vivo signal in figure 3.26 and its peak amplitude has been 9.4 mV corresponding to the invasive blood glucose level of 94 mg/dl respectively.

This preliminary in-vivo observation shows that the peak amplitude in FFT domain responses with respect to blood glucose levels and resembles our in-vitro findings.

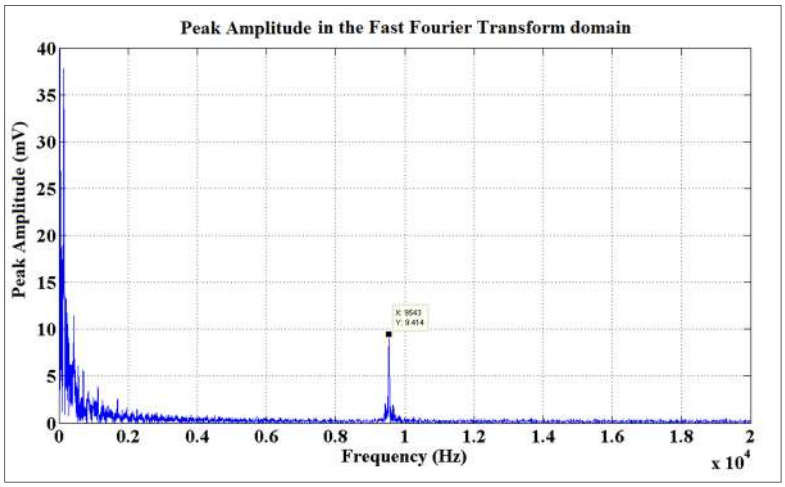

Figure 3.27: The peak amplitude (mV) spectrum in the FFT domain.

Further, extended in-vivo clinical study performed to explore the practicable relation of this peak amplitude in FFT domain with respect to the actual blood glucose concentration.

3.7.1 Extended in-vivo clinical study:

In this extended in-vivo clinical study, the role of amplitude-modulated ultrasound (absence and presence) with infrared light-based technique are studied. Further, our observed signal analysis in FFT domain performed to analyze peak amplitude relation with the reference (invasive) blood glucose levels. As this relation will assist in performing calibration aspects for our noninvasive technique based in-vivo blood glucose measurements.

3.7.2 Study subjects:

In total five healthy adult subjects (four males and one female) participated in this clinical study. All the five subjects are healthy normal (age = 27±03 years, height = 158±4.0 cm, weight = 64.8±1.6 kg, and, Random Blood Glucose Level = 90±5.0 mg/dl). The clinical study reported here are in accordance with the standard ethical

procedures and performed with the informed consent of all the respective study subjects. The Ethical committee of IMS-BHU,Varanasi approved the clinical study.

3.7.3 Experimental phases:

The experimental phases include:

3.7.3.1 Phase I (a): Before meal intake session in absence of amplitude modulated ultrasound in our prototype:

In this phase, the ultrasound modules in our prototype are in OFF mode. Only the Infrared modules consisting of light source and detector are in ON mode. Now, as per instructions, one by one, all the study subjects (before meal intake) place their respective index finger within the finger holder of the prototype unit.

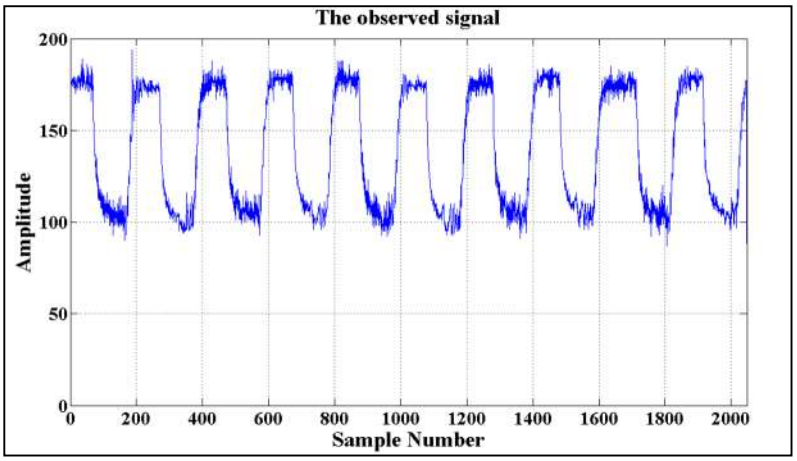

Figure 3.28: The observed signal of the study subject in absence of amplitude-modulated ultrasound in our noninvasive technique based prototype during before meal intake session

Subsequently, for analysis purpose, acquisition of all the output signals performed during Ultrasound unit-OFF and Infrared unit-ON mode. The figure 3.28 and 3.29 depicts one sample observed signal and its respective spectrum in FFT domain.

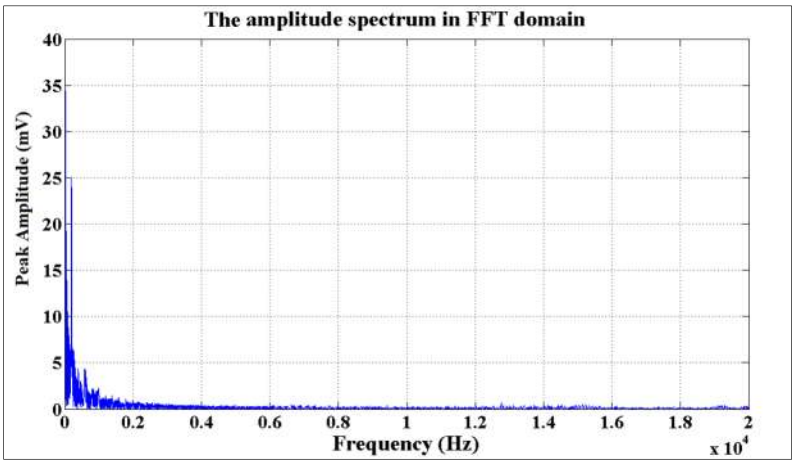

Figure 3.29: The observed peak amplitude spectrum from the study subject in absence of amplitude-modulated ultrasound in our noninvasive technique based prototype during before meal intake session

3.7.3.2 Phase I (b): Before meal intake session in presence of amplitude modulated ultrasound in our prototype:

During this phase both, the amplitude modulated ultrasound and infrared modules in our prototype are in ON mode. Again, as per instructions, one by one, all the study subjects (before meal intake) place their respective index finger within the finger holder of the prototype unit.

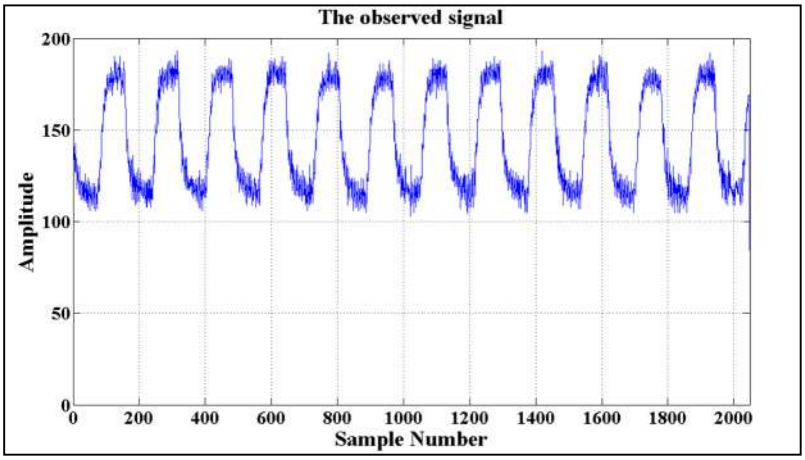

Figure 3.30: The observed signal from the study subject in presence of amplitude-modulated ultrasound in our prototype during before meal intake session.

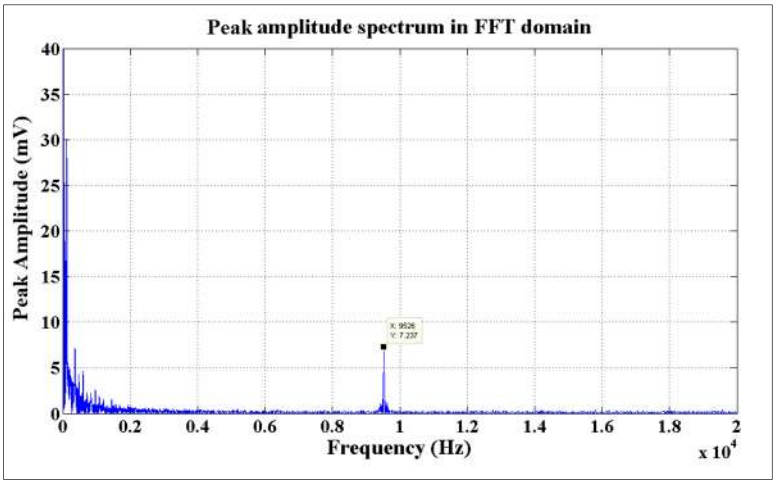

Figure 3.31: The observed peak amplitude spectrum from the study subject in presence of amplitude-modulated ultrasound in our noninvasive technique based prototype during before meal intake session

Subsequently, for analysis purpose, acquisition of all the output signals performed during Ultrasound unit-ON and Infrared unit-ON mode. The figure 3.30 and 3.31 depicts one sample observed signal (of subject 2) and its respective spectrum in FFT domain.

3.7.3.3 Phase II: One hour after meal intake session in presence of amplitude modulated ultrasound in our prototype:

Correspondingly, as in Phase I (b), during this phase both, the amplitude modulated ultrasound and infrared modules in our prototype are in ON mode.

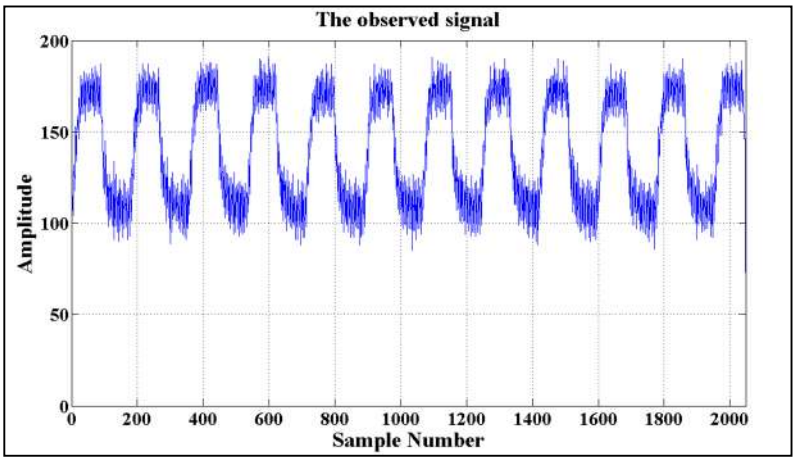

Figure 3.32: The observed peak amplitude spectrum from the study subject in presence of amplitude-modulated ultrasound in our noninvasive technique based prototype during one hour after meal intake session.

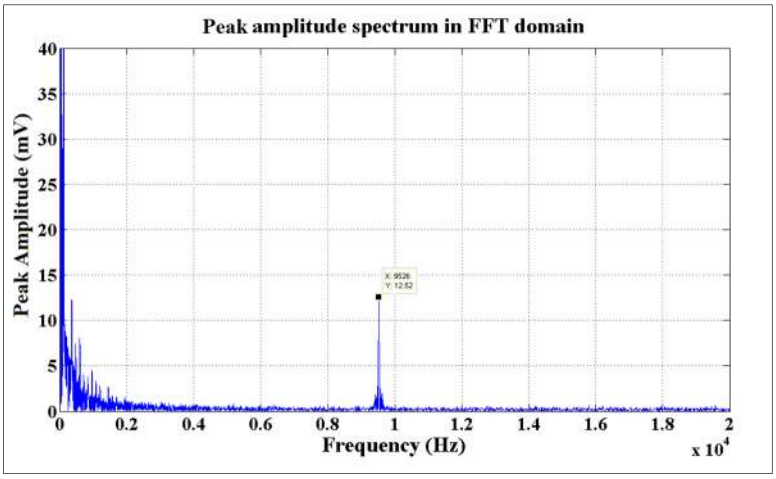

Figure 3.33: The observed peak amplitude spectrum from the study subject in presence of amplitude-modulated ultrasound in our noninvasive technique based prototype during one hour after meal intake session

Again, as per instructions, one by one, all the study subjects (one hour after meal intake) place their respective index finger within the finger holder of the prototype unit. Subsequently, for analysis purpose, acquisition of all the output signals performed during Ultrasound unit-ON and Infrared unit-ON mode. The figure 3.32 and 3.33 depicts the one sample observed signal (of subject 2) and its respective spectrum in FFT domain.

The figure 3.32 depicts the simultaneous invasive blood glucose readings of all the study subjects as acquired using the invasive glucometer (Accu-Chek Active of Roche Diagnostics GmbH, Mannheim, Germany).

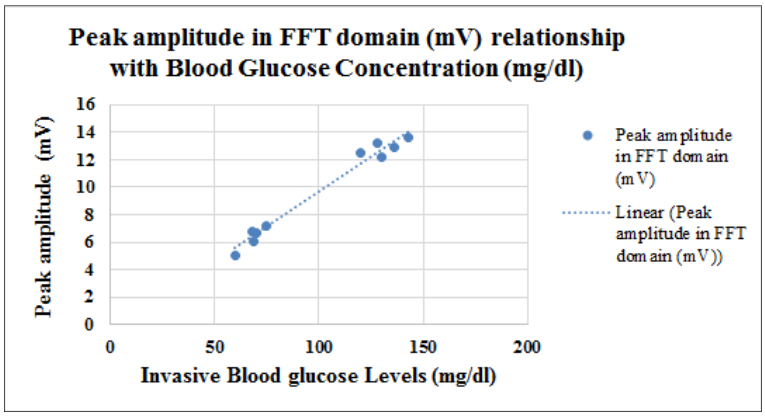

Figure 3.34: The in-vivo signals based peak amplitude spectral variations in the FFT domain with respect to change in the blood glucose levels during fasting and 2-hour postprandial stages.

3.7.4 Result analysis:

The figures 3.28 and 3.29 depicts that during before meal intake session in the absence of amplitude-modulated ultrasound in our prototype, no observation of peak amplitude (mV) in the FFT domain. But in contrary, during before and after meal intake sessions in presence of amplitude modulated ultrasound in our prototype, the observed signal as depicted from figures 3.30, 3.31 and 3.32, 3.33 of Subject 2 yields 7.2 mV and 12.5 mV as peak amplitude in the FFT domain respectively. Hence, this aspect proves the role of amplitude-modulated ultrasound in generating blood glucose concentration based corresponding peaks amplitude in the FFT domain.

Again, the simultaneous blood glucose levels of Subject 2 as measured during both the sessions are 75 mg/dl and 120 mg/dl respectively. This indicates increase in blood glucose level (75 mg/dl to 120 mg/dl) due to meal intake and correspondingly peak amplitude also increases (from 7.2 mV to 12.5 mV) by acting as an indicator for this respective (blood glucose level change) response. This entire phenomenon proves the promising efficiency of our noninvasive technique for blood glucose detection in the human subjects. Similarly, when all the data obtained from the subjects (1 to 5) has been computed in figure 3.34, it depicts that pattern of change in peak amplitude values (in FFT domain) correspondingly changes with the change in the Invasive (reference) blood glucose data as acquired by using the invasive glucometer (Accu-Chek Active of Roche Diagnostics GmbH, Mannheim, Germany). This correlated change in peak amplitude in FFT domain in in-vivo experiments resembles our earlier in-vitro experiments.

3.8 Calibration:

By correlating this type of observations (in-vitro and in-vivo) as depicted in figures 3.24, 3.25 and 3.34, we have arrived at the concept that the peak amplitude (mV) in FFT domain varies corresponding to the change in blood glucose levels. Hence, these peak amplitude values in FFT domain calibrate our noninvasive technique based prototype unit measurements to predict the sample glucose concentration.

Now, by assuming this relationship as linear, its mathematical expression is:

$$P_{amplitude} = mG_c + C \qquad \text{Equation (14)}$$

Where, $P_{amplitude}$ stands for peak amplitude in FFT domain, m and G_c are slope and intercept of the straight line representing this linear relationship. Their values are

derived utilizing two noninvasive measurements, $P_{amplitude1}$ and $P_{amplitude2}$, taken at known glucose concentrations (two point calibration for more accuracy), G_{c1} and G_{c2}, as follows:

$$m = \frac{P_{amplitude1} - P_{amplitude2}}{G_{c1} - G_{c2}} \quad \text{Equation (15.1)}$$

$C = P_{amplitude1} - mG_{c1}$, and $C = P_{amplitude2} - mG_{c2}$ Equation (15.2)

The values of m and C applied to calibrate our noninvasive measurements made thereafter to achieve the prediction of the glucose concentration, $G_{c_{prediction}}$, as follows:

$$G_{c_{prediction}} = \frac{P_{amplitude} - C}{m} \quad \text{Equation (16)}$$

Herein, from the equation 14 to equation 16 forms the basis in preparing the Look-up Table for (provided in Appendix III) converting the peak amplitude (mV) in FFT domain to the corresponding Predicted (Noninvasive) Blood Glucose Levels (P-BGL) in mg/dl. In this present work, two-point calibration method adopted [Vaddiraju *et al.* (2010)], in which we calibrate our prototype using two known glucose concentrations for attaining higher accuracy in reference (invasive) blood glucose estimations.

Afterwards, the calibration was applied and the predicted (noninvasive) glucose values acquired from our noninvasive measurements were compared to reference (invasive) blood glucose measurements performed concurrently to check the accuracy of the proposed noninvasive technique.

3.9 Inference:

Hence, this section reports the glucose concentration related sensitivity of our noninvasive approach. The effective correlation between the trends of peak amplitude (mV) in FFT domain spectrum with changing blood glucose levels proves the practicability of this new approach. By adopting such phenomenon, we performed various noninvasive blood glucose measurement based clinical studies in human subjects and reported in the chapter-5 of this present thesis.

3.10 Tests methodology:

Establishing clinical accuracy and competence of the noninvasive technique is a multifaceted job. In order to check our noninvasive technique, we have performed

clinical studies that includes OGTT (Oral Glucose Tolerance Tests), Fasting-Postprandial-Random Tests on normal, pre-diabetic and diabetic study subjects. Further, our clinical study correlates blood glucose levels relationship with blood pressure and Glycated hemoglobin levels. All the clinical investigations reported in this present thesis were performed under the expert consultation, observation of Dr. Neeraj Kumar Agarwal, Diabetologist and Associate Professor, Department of Endocrinology and Metabolism, Institute of Medical Sciences, Banaras Hindu University, Varanasi, Uttar Pradesh. The figure 3.35 presents the snapshot of the Accu-Check Active Invasive Glucometer of Roche Diagnostics GmbH, Mannheim, Germany. Further, Roche Diagnostics, GmbH, Mannheim, Germany assessed the accuracy of the Accu-Chek Active system as per the ISO (International Organization for Standardization) 15197, and the Accu-Chek Active system meets the accuracy requirement for the ISO 15197 standard [ISO_Active_EN, (2006); Lam (2008)].

Henceforth, in this present work, for Invasive Blood Glucose Level measurement (referred here as the Reference Blood Glucose Level) in study subjects the above-mentioned invasive glucometer is used.

Figure 3.35: Accu-Chek Active of Roche Diagnostics GmbH, Mannheim, Germany (Invasive Glucometer) for Reference Blood Glucose Level measurement in human subjects;

1. Test strip cylindrical box; **2.** Test strip box pack; **3.** Test strips; **4.** Skin pricking needles; **5.** Skin/finger pricking device; **6.** Invasive Glucometer; **7.** Complete box-pack.

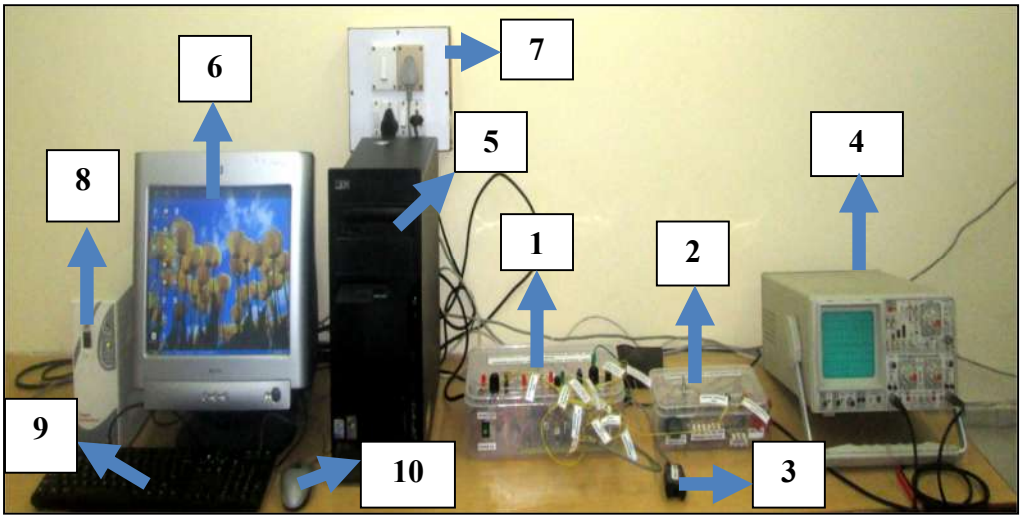

Figure 3.36: Our Noninvasive technique based prototype (MUS-IR) unit;

1: Modulating wave supply unit and MUS-IR unit; **2:** Carrier wave supply unit; **3:** Finger holder probe; **4:** Oscilloscope. **5:** Central Processing Unit; **6:** Computer display; **7:** Main Power Supply; **8:** Uninterrupted power supply; **9:** Keyboard; **10:** Computer Mouse

The figure 3.36 represents our prototype unit snapshot for noninvasive blood glucose measurement. Similarly, the figure 3.37 presents the snapshot of our noninvasive technique based prototype unit during blood glucose measurement processes.

In this present work, for noninvasive Blood Glucose Level measurement (referred here as the Predicted Blood Glucose Level) in study subjects the above-mentioned noninvasive technique based prototype unit is used.

The Ethical Committee of Institute of Medical Sciences, Banaras Hindu University, Varanasi, ethically approved all the human studies mentioned in this present thesis work.

Further, invasive, and noninvasive blood glucose measurements of all the study subjects as reported in this present thesis were performed under the controlled conditions of temperature and humidity respectively.

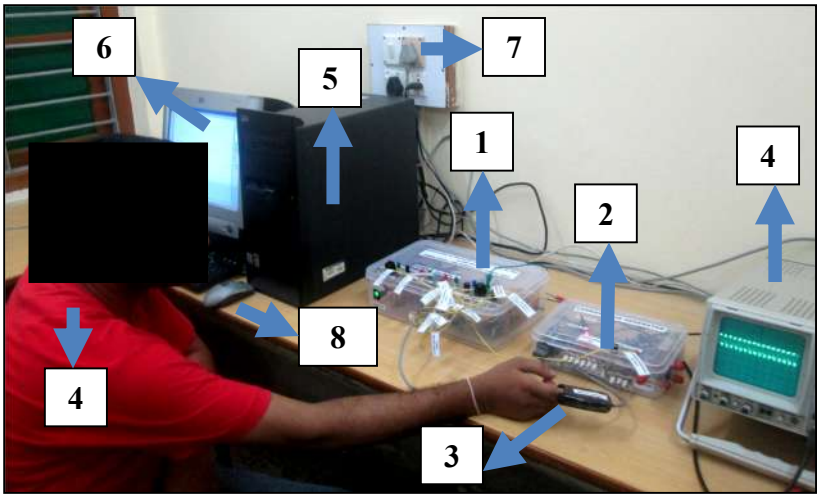

Figure 3.37: Our noninvasive technique based prototype unit for Predicted (Noninvasive) Blood Glucose Level measurement in human subjects;

1: Modulating wave supply unit and MUS-IR unit; **2:** Carrier wave supply unit; **3:** Finger holder probe; **4:** Signal acquisition by an oscilloscope and exporting it to the computer for Predicted (noninvasive) Blood Glucose Level measurement **5:** Central Processing Unit; **6:** Spectral reading program with computer display unit; **7:** Main Power Supply; **8:** Keyboard and Computer Mouse.

3.11 Clarke Error Grid analysis:

The Clarke Error Grid analysis has been the universal approach for evaluating medical significance of the developing glucose sensor (mostly noninvasive) based techniques for blood glucose determination.

In this present work, the Clarke Error Grid Analysis critically evaluates the medical importance of the differences between our noninvasive (as predicted by our prototype unit) technique based blood glucose levels as the predicted method under examination and invasive glucometer (Accu-Chek Active of Roche Diagnostics GmbH, Mannheim, Germany) based blood glucose level measurement as the reference method.

Clarke *et al.* (1987) presented this methodology using the Cartesian diagram to compute the predicted (noninvasive) blood glucose values against the reference (invasive) blood glucose values. For instance, when the noninvasive (predicted) blood glucose value is 123 mg/dl and the reference (invasive) blood glucose value obtained is 88 mg/dl, the Cartesian XY coordinates represents it as (88,123) respectively. In this fashion, the diagonal line where X=Y, expresses the ideal measurements. The data points below and above the diagonal line represents the overestimation and underestimation of

the real blood glucose values respectively. Further, when any data pair fall over the borderline of any zones, the nearness of its (X, Y) coordinate towards either zone determines its zone of occupancy [Hidalgo *et al.* (2014); Clarke *et al.* (1987)].

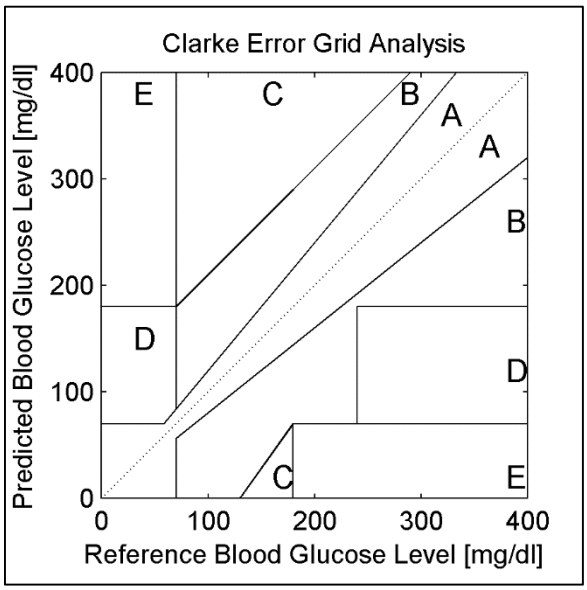

Figure 3.38: Clarke Error Grid plot [Clarke *et al.* (1987)].

Further, based on the degree of miss calculation, the XY- Cartesian graph consists different grid zones.

As shown in figure 3.38, the Clarke Error Grid consist of five different zones in the XY-Cartesian graph with the following interpretations [Hidalgo *et al.* (2014); Clarke *et al.* (1987)].

Zone A [Medically accurate]: Characterizes the blood glucose values that diverge away from the actual reference values by means of 20 % or less. This zone also includes hypoglycemic blood glucose values (less than 70 mg/dl). The output values in this zones are medically correct and medical attention will be proper [Hidalgo *et al.* (2014); Clarke *et al.* (1987)].

Zone B [Medically acceptable]: Characterizes the blood glucose values that diverge from the actual reference values by means of more than 20%. This domain represents the starting of errors but medical treatment has a high possibility of being accurate. The data points under the Zone B are also medically significant and tolerable [Hidalgo *et al.* (2014); Clarke *et al.* (1987)].

Zone C-E [Medically insignificant and potentially dangerous]: The blood glucose values in those zones represents potentially dangerous and unacceptable measurements. As the predicted values are far away from the reference values, the medical treatment based on these results will be erroneous and involves high risk [Hidalgo *et al.* (2014); Clarke *et al.* (1987)].

3.12 Statistical analysis:

In this present work, various statistical performance metrics based parameters executes accuracy measure analysis for correlating actual invasive blood glucose levels with the estimated noninvasive blood glucose levels and yields promising results.

Herein, various statistical performance assessment parameters mainly includes (i) Mean Absolute Error (MAE), (ii) Median Absolute Error (MdAE), (iii) Root Mean Squared Error (RMSE), (iv) Percentage of Mean Absolute Relative Error (%MARE), (v) Percentage of Median Absolute Relative Error (%MdARE), (vi) SEP (Standard Error of Prediction) (vii) r value (Pearson Correlation Coefficient).

The Table 3.12 represents the mathematical expressions of the performance assessment parameters utilized in this present work for the total number of sample data pairs obtained during our clinical investigations. All these accuracy measure evaluates the correctness of predicted noninvasive blood glucose levels with respect to the reference invasive blood glucose levels.

Further, to assess the statistical significance of our results various statistical analysis methods Clarke and Parkes Error Grids, Accuracy measure, Rank correlation, Bland Altman plot, Mountain plot, Independent sample t tests, CUSUM test for linearity, and Deming Regression are applied over our total clinical study based results.

Table 3.12: Performance assessment parameters

Accuracy Measure	Mathematical Expression	Symbol Notations	References
MAE (Mean Absolute Error)	$MAE = \frac{\sum_{i=1}^{n}\lvert y_i - \hat{y}_i\rvert}{n}$	Where y_i is the Reference Blood Glucose Level (RBGL) value, $\hat{y}_i$ is the Predicted Blood Glucose Level (PBGL) value, and n represents the total number of sample pairs.	Hariri *et al.* (2013); Shcherbakov *et al.* (2013); Guevara *et al.* (2010); Facchinetti *et al.* (2007).
MdAE (Median Absolute Error)	$MdAE = median\sum_{i=1}^{n}\lvert y_i - \hat{y}_i\rvert$		
RMSE (Root Mean Squared Error)	$RMSE = \sqrt{\frac{\sum_{i=1}^{n}(y_i - \hat{y}_i)^2}{n}}$		
%MARE (Percentage of Mean Absolute Relative Error)	$MAPE = \frac{\sum_{i=1}^{n}\left\lvert\frac{y_i - \hat{y}_i}{y_i}\right\rvert \times 100}{n}$		
%MdARE (Percentage of Median Absolute Relative Error)	$MdAPE = median\sum_{i=1}^{n}\left\lvert\frac{y_i - \hat{y}_i}{y_i}\right\rvert \times 100$		
SEP (Standard Error of Prediction)	The equation for the standard error of the predicted y is: $\sqrt{\frac{1}{(n-2)}\left[\sum(y-\hat{y})^2 - \frac{[\sum(x-\hat{x})(y-\hat{y})]^2}{\sum(x-\hat{x})^2}\right]}$	Where x and y are the sample means AVERAGE (known_x's) and AVERAGE (known_y's), and n is the sample size.	Bill (2013)
r value (Pearson Correlation Coefficient)	The correlation (r) between x and y is: $r = \frac{1}{n-1}\sum_{i=1}^{n}\left(\frac{x_i - \bar{x}}{s_x}\right)\left(\frac{y_i - \bar{y}}{s_y}\right)$ $= \frac{\sum_{i=1}^{n}(x_i - \bar{x})(y_i - \bar{y})}{\sqrt{\sum_{1=1}^{n}(x_i - \bar{x})^2(y_i - \bar{y})^2}}$	Where x represents RBGL value, y represent PBGL value and, n represents the total number of sample pairs. The mean and standard deviations of the two variables are $\bar{x}$ and s_x for x values, and $\bar{y}$ and s_y for y values.	Sharma (2012)